Search for exotic states in $e^+e^- \to p\bar{p}\omega$ at center-of-mass energies above 4 GeV at BES III

Frederik Weidner

Master Thesis
in the Department of Physics
at the WWU Münster
October 8, 2018

Contents

1 Introduction

Ever since ancient times people have been trying to figure out what the world around us is made of. The idea that the world is built up from discrete indivisible particles has been around as a concept in philosophy already by the ancient Greeks. Since then we have come a long way to the first evidences of the atom in the 1800s [Dal42]. Later experiments by Rutherford and others [Rut11] showed that the atom which was considered indivisible consists of a nucleus and an atomic shell. Not much later, it was discovered that the nucleus consists of protons and neutrons [NV17] and that the shell is built up from electrons [Ast20]. In the modern times of particle physics, the standard model has been developed to explain many but not all of the features of particles in the universe. One part of the standard model is quantum chromodynamics (QCD) which describes the interaction of quarks and gluons. These among other things build up the protons and neutrons. The quarks and gluons carry a so called color charge and QCD predicts a behavior called confinement which allows only color neutral states to exist. This can for example be achieved by three quarks with different colors or a quark antiquark pair with a color and corresponding anticolor. Particles built up from three quarks or three antiquarks are called (anti-) baryons and particles built up from a quark and an antiquark are called mesons. Additionally to these two kind of particles, for which much evidence has been found, in theory more combinations are possible. These are called exotic states and could be states consisting of more quarks or even have a gluon as a constituent particle.
To get a deeper understanding of the standard model larger and more complex experiments are needed. A big part of the research in particle physics is done in particle accelerators one of which is the BEPCII in Beijing. BEPCII accelerates electrons and positrons and brings them to collision inside the BESIII experiment. The BESIII experiment was built for the purpose of τ- and charm- physics and has produced many important contributions to this aspect of the standard model. One part of charm physics is the investigation of the charmonium spectrum. A

charmonium state is built up from a charm and an anticharm quark and in principle its properties can be calculated from QCD with some approximations. During the measurement of the charmonium spectrum, particles were found that could not be described as a charmonium state, like the X(3872) that was found in 2003 [C$^+$03]. Another possibly exotic state in the charmonium region is the Y(4260) that was discovered two years later [A$^+$05b]. The reason why these particles are believed to be exotic is because their decay pattern does not fit into the expectations for a charmonium state at the corresponding masses or they are simply supernumerary. Additional research on the Y(4260) particle showed that the spectra produced by the particle might in fact be the result of two particles Y(4220) and Y(4320) that overlap [A$^+$17b].

To get additional information on this puzzle, the reaction $e^+e^- \to p\bar{p}\omega$ is investigated in this thesis. This is done to see whether there are contributions of the Y(4260) decaying to $p\bar{p}\omega$. In order to do this, data that has been taken in the energy region $4.0\,\text{GeV} \leq \sqrt{s} \leq 4.6\,\text{GeV}$ in the period between 2011 and 2017 by the BESIII experiment is analyzed. Criteria are developed to get data samples with preferably low background. These data samples are then used to look at spectra of the subsystems to identify underlying production processes. In the end, the cross section of this process is calculated for the first time and a search for (exotic) resonances in $e^+e^- \to Y \to p\bar{p}\omega$ is conducted. No significant signal is observed and consequently upper limits are derived, both for the Y(4260) decay to $p\bar{p}\omega$ and for other possible exotic states Y.

2 Theory

To understand the theoretical nature of the analyzed reaction many different models have to be considered. The most used model is the Standard Model of particle physics.

2.1 Standard Model of particle physics

The Standard Model of particle physics contains several particles that are displayed in Figure 2.1. Furthermore, for each particle there is an oppositely charged antiparticle. On the one hand there are fermions which have a spin of $s = 1/2$ and on the other hand there are bosons with integer spin.
Bosons with a spin of $s = 1$ are called gauge bosons and are the carriers of the fundamental forces: The photon for the electromagnetic force, the gluon for the strong force and the $Z^0/W^{\pm}$ bosons for the weak force. Additionally there is the Higgs boson which is scalar ($s = 0$) and is the reason for the mass of the quarks, the mass of the charged leptons and the mass of the gauge bosons [Ele18].
Fermions are divided into leptons (electron, muon, tau and the corresponding neutrinos) and quarks (**u**p, **d**own, **c**harm, **s**trange, **t**op, **b**ottom) and form the conventional matter. The main difference between these two kind of particles is that quarks cannot exist as free particles, which can be explained by quantum chromodynamics (QCD), the theory of the strong interaction. In QCD, quarks carry a so called color charge which can either be red, green or blue and antiquarks carry the corresponding anticolors. Leptons do not carry such a color charge. The strong interaction allows only color neutral states, so called hadrons, to be observed freely. This feature of QCD is called confinement. In this model there are several possibilities for hadrons to be build up from quarks and antiquarks. The conventional hadrons are (anti)baryons (see Section 2.1.1), consisting of three (anti)quarks and mesons (see Section 2.1.2), consisting of a quark and an antiquark. Additionally, QCD predicts so called exotic states (see Section 2.2) which are neither of the former two alternatives [Ele18].

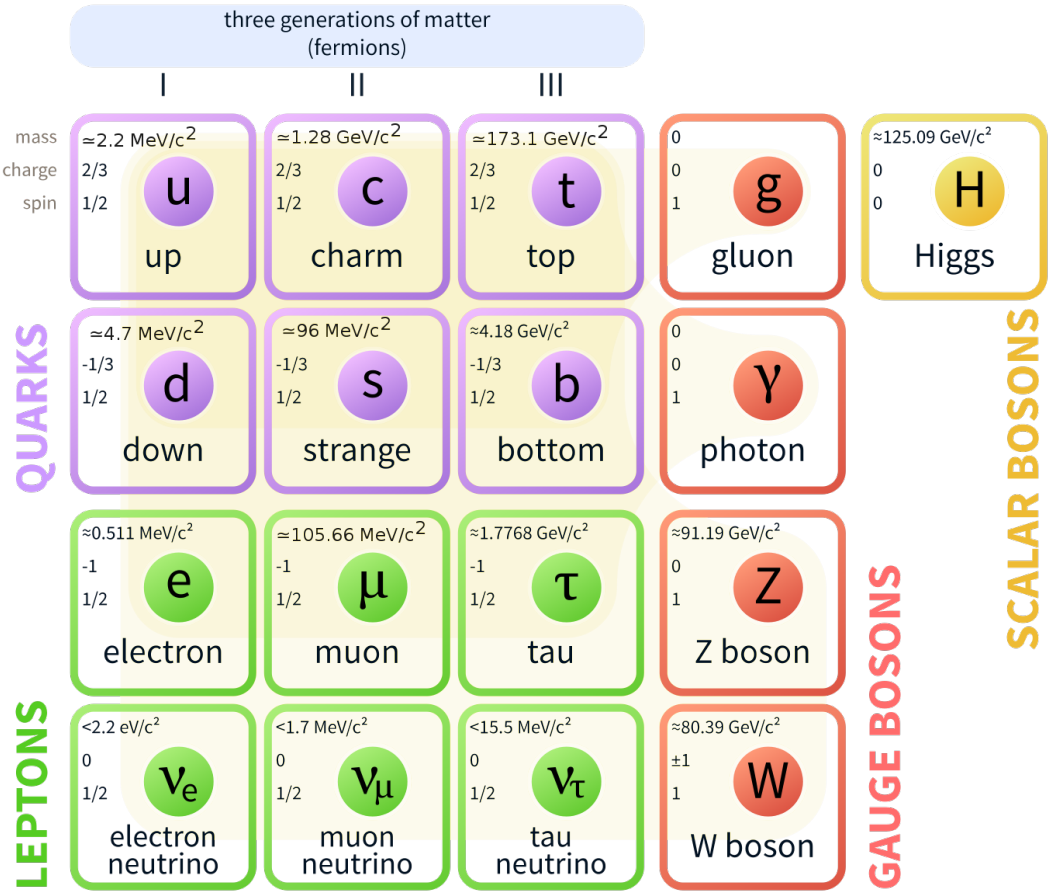

Figure 2.1 – The Standard Model of particle physics consisting of six quarks, six leptons, five gauge bosons and the Higgs boson [Mis06]. In the top left corner the values for mass, charge and spin are listed [T+18]. The masses of the neutrinos are part of physics beyond the standard model.

To systematically examine both the particles of the Standard Model and composite particles it is useful to define some properties of the particles, these are called quantum numbers. An important quantum is the parity P which describes the behavior of the particles wave function under spatial point reflection. It can have eigenvalues of $P = \pm 1$. For particles which are their own antiparticles, it is also possible to define the so called charge parity (C parity), which describes the behavior of the particles wave function when exchanging particles with their corresponding antiparticles. The C parity also has eigenvalues of $C = \pm 1$.
Additionally there are the so called flavor quantum numbers isospin T_3, strangeness S, charm C, bottomness B' and topness T. The isospin is a quantum number corresponding to the up and down quark with

$$\begin{aligned} T_3(\mathrm{u}) &= +\frac{1}{2}, \quad T_3(\mathrm{d}) = -\frac{1}{2} \quad \text{and} \\ T_3\left(\overline{\mathrm{u}}\right) &= -\frac{1}{2}, \quad T_3\left(\overline{\mathrm{d}}\right) = +\frac{1}{2}. \end{aligned} \tag{2.1}$$

The strangeness S is the quantum number for the strange quark with

$$S(\mathrm{s}) = -1 \quad \text{and} \quad S(\overline{\mathrm{s}}) = +1. \tag{2.2}$$

C, B' and T are defined similarly [Dem10].
In a composite state the constituents can have an angular momentum L relative to each other. Together with the spin s the particle has a total angular momentum of $\vec{J} = \vec{s} + \vec{L}$.

2.1.1 Baryons

A baryon consists of three quarks forming a color neutral state. Since quarks carry a spin of $s = 1/2$, for a baryon the spin can either couple to $s = 1/2$ or $s = 3/2$. The particles build up from quarks can be sorted into so called multiplet. In these multiplets the particles are categorized according to their quantum numbers. The multiplets containing baryons build up from the three lightest quarks are shown in Figure 2.2. Here, on the axes the third component of the isospin T_3 and the strangeness S are shown.

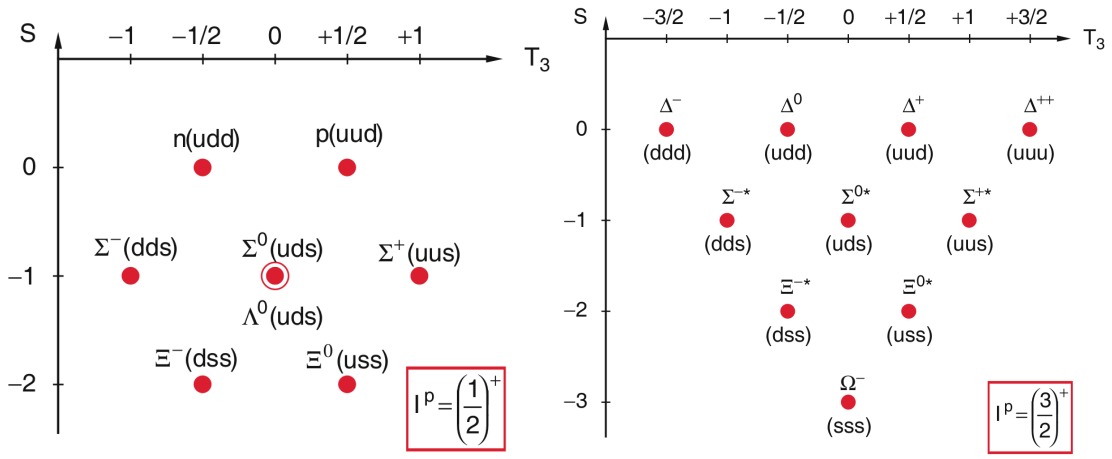

(a) Baryon octet with $J = 1/2$ and $P = +1$. **(b)** Baryon decuplet with $J = 3/2$ and $P = +1$.

Figure 2.2 – Baryon multiplets made from u-, d- and s-quarks. On the abscissa the third component of the isospin T_3 and on the ordinate the strangeness S is shown. The particles are indicated by a dot (or circle) including their name and quark content [Dem10].

Following group theory and the Pauli exclusion principle there are eight possible ground state baryons with a spin of $s = 1/2$ and ten with a spin of $s = 3/2$, each with an angular momentum of $L = 0$. The $J = 1/2$ octet also contains the two well-known nucleons (proton p and neutron n), which form the nuclei of the matter surrounding us. In Table 2.1 some of the properties of the proton are listed. For a baryon the parity P can be calculated via [Won98]

$$P = (-1)^L. \tag{2.3}$$

Table 2.1 – Properties of the proton. All values taken from [T+18].

	p
Quark content	uud
Mass m	$(938.272\,081 \pm 0.000\,006)\,\mathrm{MeV/c^2}$
Life time τ	$> 2.1 \times 10^{29}$ years
Charge Q	0
Isospin T	$1/2$
Isospin T_3	$+1/2$
Strangeness S	0
Total angular momentum J	$1/2$
Parity P	+1

2.1.2 Mesons

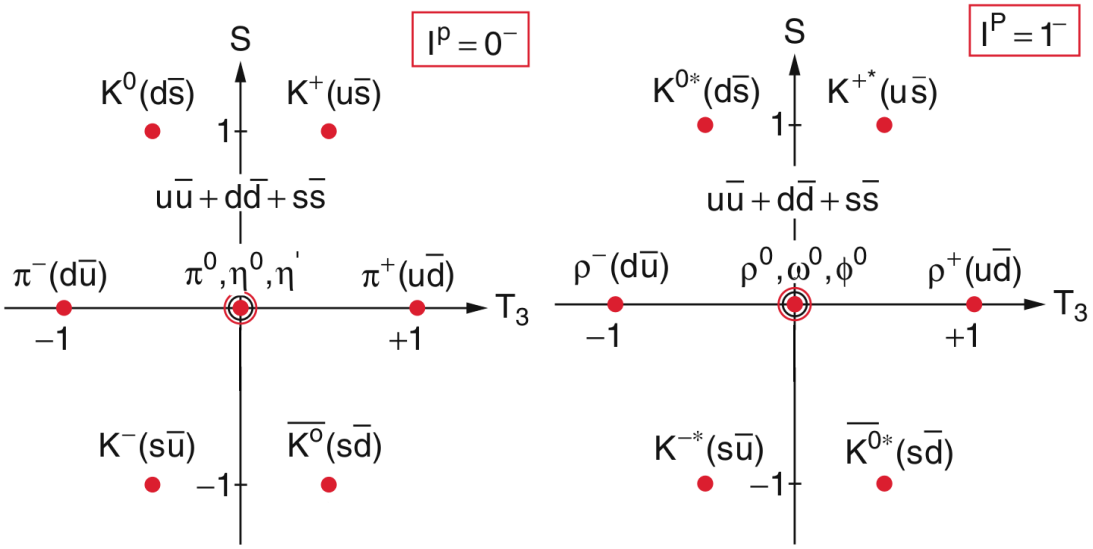

(a) Meson nonet with $J = 0$ and $P = -1$. **(b)** Meson nonet with $J = 1$ and $P = -1$.

Figure 2.3 – Meson multiplets made from u-, d- and s-quarks. On the abscissa the third component of the isospin T_3 and on the ordinate the strangeness S is shown. The particles are indicated by a dot (or circle) including their name and quark content [Dem10], edited.

A meson is a state consisting of a quark and an antiquark. Here the spin of the quark and antiquark can couple to either $s = 0$ or $s = 1$. With an angular momentum of $L = 0$ these mesons are called pseudoscalar ($J^P = 0^-$) or vector mesons ($J^P = 1^-$). The corresponding multiplets are shown in Figure 2.3. An example for a vector meson is the ω meson, which also plays a role in the analyzed reaction. In Table 2.2 some of the properties of the ω are listed. Because of the relatively short life time of the ω meson of $\tau = (7.75 \pm 0.07) \times 10^{-23}\,\mathrm{s}$ [T+18], it can only be detected indirectly via its decay particles. The main decay channel of the ω meson with a branching ratio of $\mathrm{BR}(\omega \to \pi^+\pi^-\pi^0) = (89.2 \pm 0.7)\,\%$ [T+18], is the decay into three pions, which are pseudoscalar mesons,

$$\omega \to \pi^+\pi^-\pi^0. \tag{2.4}$$

The second most common decay is the decay

$$\omega \to \pi^0\gamma \tag{2.5}$$

with a branching ratio of $\mathrm{BR}(\omega \to \pi^0\gamma) = (8.40 \pm 0.22)\,\%$ [T+18].

In Table 2.3 some of the properties of the pions are listed. The π^0 coming from the ω decay is also detected via its decay particles. Here the main decay channel is

$$\pi^0 \to \gamma\gamma \tag{2.6}$$

with $\mathrm{BR}(\pi^0 \to \gamma\gamma) = (98.823 \pm 0.034)\,\%$ [T$^+$18].
At higher energies additional quarks come into play, which can also form hadrons. In this thesis the charmonium mesons, which are built up from a c and $\overline{\mathrm{c}}$ quark, play an important role and they are described in detail in Section 2.2.
Tables 2.2 and 2.3 also contain the parity P which can be calculated for a meson, via [T$^+$18]

$$P = (-1)^{L+1}. \tag{2.7}$$

Additionally for mesons which are their own antiparticles the C parity can be calculated via [T$^+$18]

$$C = (-1)^{L+S}. \tag{2.8}$$

This means that some combination of quantum numbers cannot be realized for mesons, which are [T$^+$18]

$$J^{PC} = 0^{--}, (\text{odd } J)^{-+}, (\text{even } J)^{+-}. \tag{2.9}$$

These quantum numbers and particles carrying them are called exotic.

Table 2.2 – Properties of the ω vector meson. All values taken from [T$^+$18].

	ω
Quark content	$\frac{1}{\sqrt{2}}\left(\mathrm{u\overline{u}} + \mathrm{d\overline{d}}\right)$
Mass m	$(782.65 \pm 0.12)\,\mathrm{MeV/c^2}$
Decay width Γ	$(8.49 \pm 0.08)\,\mathrm{MeV/c^2}$
Life time τ	$(7.75 \pm 0.07) \times 10^{-23}\,\mathrm{s}$
Charge Q	0
Isospin T	0
Isospin T_3	0
Strangeness S	0
Total angular momentum J	1
Parity P	-1
Parity C	-1

Table 2.3 – Properties of the pseudoscalar π mesons. All values taken from [T+18].

	π^+ / π^-	π^0
Quark content	$u\bar{d}$ / $d\bar{u}$	$\frac{1}{\sqrt{2}}\left(u\bar{u} - d\bar{d}\right)$
Mass m	$(139.570\,61 \pm 0.000\,24)\,\mathrm{MeV/c^2}$	$(134.9770 \pm 0.0005)\,\mathrm{MeV/c^2}$
Life time τ	$(2.6033 \pm 0.0005) \times 10^{-8}\,\mathrm{s}$	$(8.52 \pm 0.18) \times 10^{-17}\,\mathrm{s}$
Charge Q	$+1$ / -1	0
Isospin T	1	1
Isospin T_3	$+1$ / -1	0
Strangeness S	0	0
Total angular momentum J	0	0
Parity P	-1	-1
Parity C	—	$+1$

2.2 Charmonium spectroscopy and exotic states

A hadron is called exotic if it has a quark content that is neither baryonic (qqq / $\overline{q}\overline{q}\overline{q}$) nor mesonic ($q\overline{q}$). Possibilities for such states would be a tetraquark ($q\overline{q}q\overline{q}$), a pentaquark ($qqqq\overline{q}$ or $q\overline{q}\overline{q}\overline{q}\overline{q}$), a hexaquark ($qqqqqq$, $qqq\overline{q}\overline{q}\overline{q}$ or $\overline{q}\overline{q}\overline{q}\overline{q}\overline{q}\overline{q}$) and more. Additionally gluons g could also play the role of a constituent and form glueballs (gg, ggg, ...) or a hybrid, which has quarks and gluons as constituents ($q\overline{q}g$, ...). For most of these states possible candidates have been found, but in many of these cases multiple explanations are possible. Examples for possibly exotic states are the so called XYZ states[1], which were found first in the context of charmonium spectroscopy. Charmonium spectroscopy is a part of hadron spectroscopy, in which the spectrum of charmonium is studied. Here especially the mass and widths as well as quantum numbers and possible decays are analyzed. In theory the spectrum of charmonium can be calculated from QCD. Because of the high mass of the charm quark (compared to u, d and s quark) the relative velocity of the two quarks in the charmonium is non-relativistic which makes it possible to use non-relativistic potentials to study the charmonium spectrum. An often used potential is the Cornell potential [CLK08]

$$V(r) = -\frac{\kappa}{r} + \sigma r \tag{2.10}$$

where κ and σ are model parameters which are determined by a fit to the experimentally found charmonium states. For small distances the Coulomb-like potential $-\frac{\kappa}{r}$ dominates, for larger distances the linear potential σr dominates which is re-

[1] Following the naming scheme used in the PDG until 2017.

sponsible for the confinement. For precise calculations relativistic corrections are applied [CLK08]. In Figure 2.4 the charmonium spectrum is shown. Here the theoretically predicted and experimentally observed charmonium states as well as predicted but yet undiscovered states are shown. Additionally Figure 2.4 shows the XYZ states in the charmonium region[2]. These states appear to have $c\bar{c}$ quark content, but do not fit in the charmonium spectrum because of quantum numbers or a decay pattern which does not fit the expectation or are just supernumerary. Many of these XYZ states are considered to be either exotic states like hybrids or tetraquarks or are some kind of molecule of loosely bound D mesons [Ols15]. The XYZ state that was discovered first is the X(3872), which was seen by the Belle experiment in 2003 as a peak in the invariant mass spectrum of $\pi^+\pi^- J/\psi$ in the decay $B \to K\pi^+\pi^- J/\psi$ [C$^+$03]. The reason why this particle is considered to be exotic is its relatively small width of $\Gamma < 1.2\,\mathrm{MeV/c^2}$ [T$^+$18], which is not to be expected for a charmonium state with its mass of $(3871.69 \pm 0.17)\,\mathrm{MeV/c^2}$ [T$^+$18], which lies above the threshold for the production of two D mesons. The decay into D mesons, which consist of a charm quark and a lighter quark (u,d,s), should be possible via the strong interaction and would lead to a much bigger decay width.
In the reaction analyzed in this thesis the annihilation of an electron and a positron is used to produce the desired final state. This leads to the fact that any directly produced state has to have the quantum numbers of the photon which are $J^{PC} = 1^{--}$. Here the Y(4260) was reported by the BaBar (B and B-bar) experiment in 2005 in the reaction $e^+e^- \to \gamma_{\mathrm{ISR}}\pi^+\pi^- J/\psi$ [A$^+$05b]. γ_{ISR} is a so called initial state radiation (ISR) photon that gets emitted by either the electron or the positron before the collision. Later the BESIII (Beijing Spectrometer III) collaboration published a fit to data on the same reaction (without the ISR photon) but with significantly improved statistics. In this fit, which can be seen in Figure 2.5, two resonances were used to describe the Y(4260) peak, which leads to a reduced mass and width of the Y(4260) [A$^+$17b]. In Table 2.4 the fit values from the BaBar experiment, the BESIII experiment, as well as the mean value calculated from the Particle Data Group (PDG) are shown. Considering the charmonium spectrum the Y(4260) is supernumerary, because in that mass region all possible $J^{PC} = 1^{--}$ states have already been found, which is the reason why it is predicted to be exotic [Ols15].

[2] In the spectrum of bottomonium, which are $b\bar{b}$ states, similar states have been found.

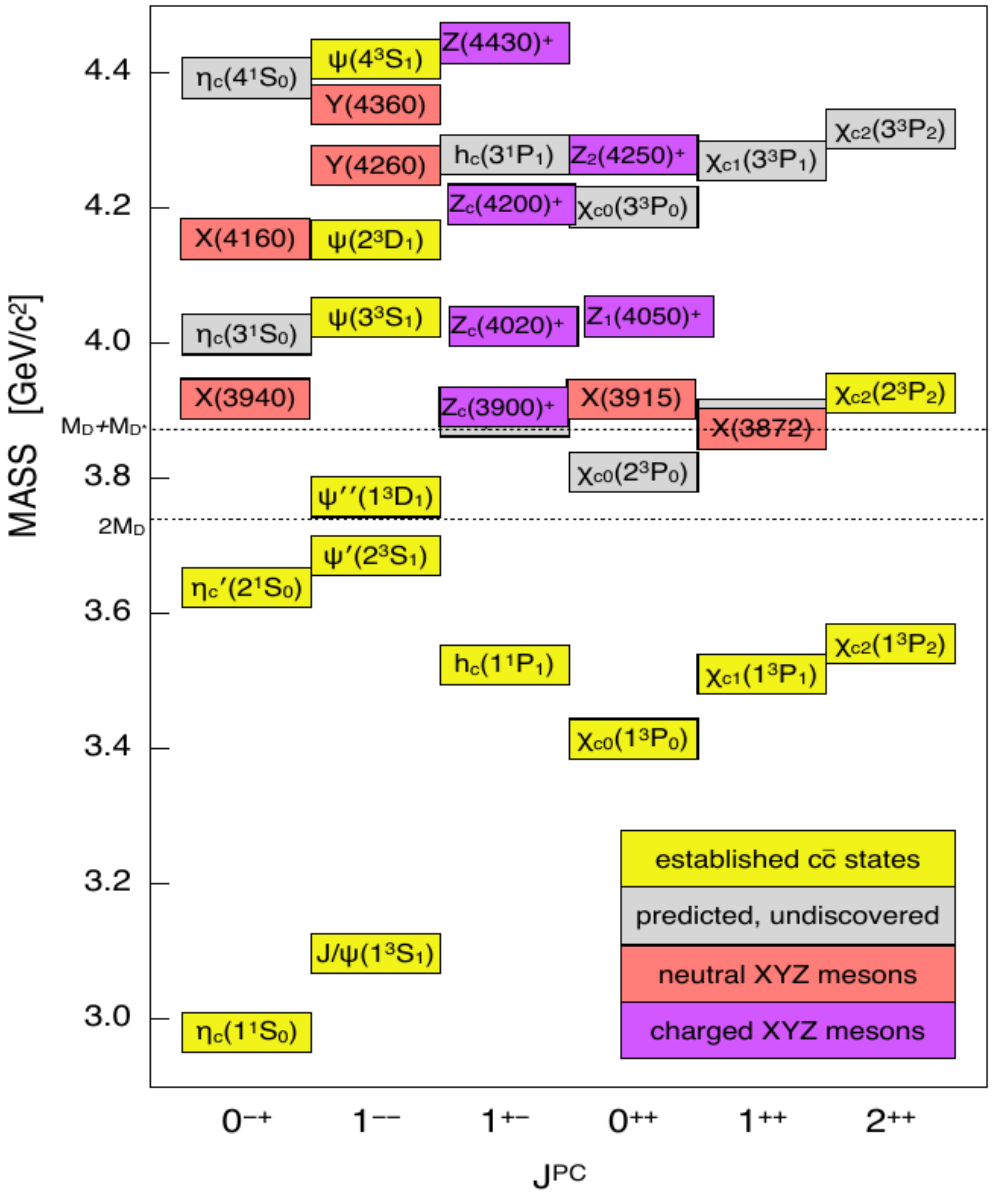

Figure 2.4 – Charmonium spectrum with the established $c\bar{c}$ states depicted in yellow, predicted but yet undiscovered charmonium states depicted in grey and XYZ states depicted in red and violet. On the abscissa the J^{PC} quantum numbers and on the ordinate the masses are shown. Additionally the threshold for the production of two D mesons and the threshold for the production of a D and D* meson are shown as a dashed line. Figure taken from [Ols15].

Table 2.4 – Fit values and properties of the Y(4260) of a fit from the BaBar collaboration, the BESIII collaboration and the mean values calculated by the PDG. Values taken from [A$^+$05b, A$^+$17b, T$^+$18].

	BaBar	BESIII	PDG
Mass m	$(4259 \pm 8^{+2}_{-6})\text{MeV/c}^2$	$(4220.0 \pm 3.1 \pm 1.4)\text{MeV/c}^2$	$(4230 \pm 8)\text{MeV/c}^2$
Decay width Γ	$(88 \pm 23^{+6}_{-4})\text{MeV/c}^2$	$(44.1 \pm 4.3 \pm 2.0)\text{MeV/c}^2$	$(55 \pm 19)\text{MeV/c}^2$
Tot. ang. momentum J	1	1	1
Parity P	-1	-1	-1
Parity C	-1	-1	-1

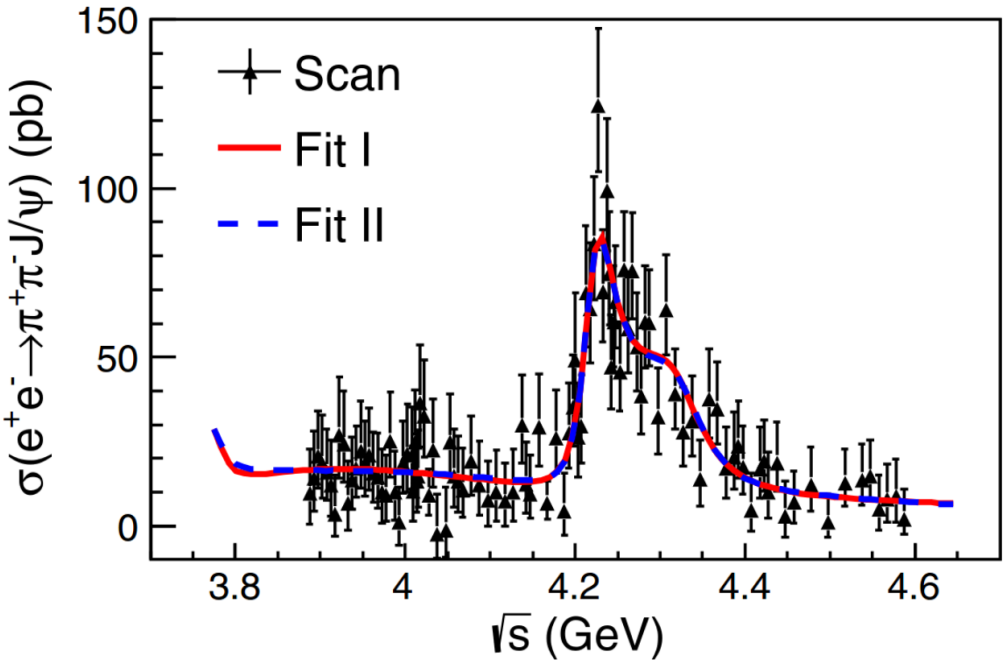

Figure 2.5 – Measured cross section σ of the reaction $e^+e^- \to \pi^+\pi^- J/\psi$ with two different fits. The fit in red was performed with a coherent sum of three Breit-Wigner functions and the one in blue was done with a coherent sum of two Breit-Wigner functions and an exponential continuum [A$^+$17b].

2.3 Born cross section

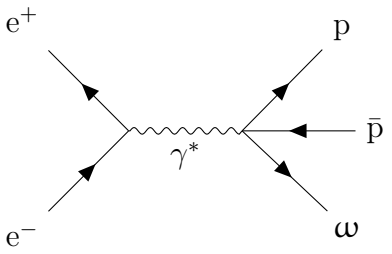

Figure 2.6 – Schematic diagram of the reaction $e^+e^- \to p\bar{p}\omega$.

One way to find evidence for a vector exotic state is the examination of the cross section of the reaction, because a resonance in the analyzed process would be visible as a certain structure in the cross section. A value that is often used in this case is the so called Born cross section σ_{Born}. For this cross section only processes of lowest order are considered, the corresponding schematic diagram is shown in Figure 2.6. In the real process, as it is measured in the experiment, also higher order diagrams contribute. On the one hand it is possible that one (or more) of the initial state particles (e^+ or e^- for the analyzed reaction) can emit a real photon (or several photons). This process is called initial state radiation and a corresponding schematic diagram is shown in Figure 2.7a. On the other hand the virtual photon can produce an electron positron pair which then annihilates again to a photon, this would be called vacuum polarization and can be seen in Figure 2.7b.
The cross section σ can be calculated from the number of events N and the integrated luminosity L_{int}:

$$\sigma = \frac{N}{L_{\text{int}}}. \tag{2.11}$$

Here L_{int} is the integral of the luminosity L over time

$$L_{\text{int}} = \int L(t)\,\mathrm{d}t. \tag{2.12}$$

To obtain the Born cross σ_{Born} section from this, correction factors for the two mentioned higher order effects have to be applied:

$$\sigma_{\text{Born}} = \frac{\sigma}{(1+\delta_{\text{r}})(1+\delta_{\text{v}})}. \tag{2.13}$$

Here $(1+\delta_r)$ is the ISR correction factor and $(1+\delta_v)$ is the vacuum polarization factor, both of which can be calculated in the theory of electromagnetic force [Jeg11, Mit14], called quantum electrodynamics (QED).
In Equation (2.11) the number of events N is used to calculate the cross section. This number can be calculated from the number of observed events N_{obs}, for the analyzed reaction, this gives:

$$N = \frac{N_{obs}}{\varepsilon \cdot \mathrm{BR}(\omega \to \pi^+\pi^-\pi^0) \cdot \mathrm{BR}(\pi^0 \to \gamma\gamma)}. \tag{2.14}$$

Here, ε is the efficiency of the analysis including the acceptance of the detector and $\mathrm{BR}(\omega \to \pi^+\pi^-\pi^0) = (89.2 \pm 0.7)\,\%$ [T$^+$18] and $\mathrm{BR}(\pi^0 \to \gamma\gamma) = (98.823 \pm 0.034)\,\%$ [T$^+$18] are the branching ratios of the decay of an ω meson into three pions and the branching ratio of the decay of the π^0 into two photons. Inserting Equations (2.11) and (2.14) in Equation (2.13) gives:

$$\sigma_{\mathrm{Born}} = \frac{N_{obs}}{L_{int} \cdot \varepsilon \cdot (1+\delta_r)(1+\delta_v) \cdot \mathrm{BR}(\omega \to \pi^+\pi^-\pi^0) \cdot \mathrm{BR}(\pi^0 \to \gamma\gamma)}. \tag{2.15}$$

To see, whether the analyzed final state is produced in resonance, this Born cross section is ploted against the center-of-mass energy, so a resonance can be seen as a structure above the continuum production.

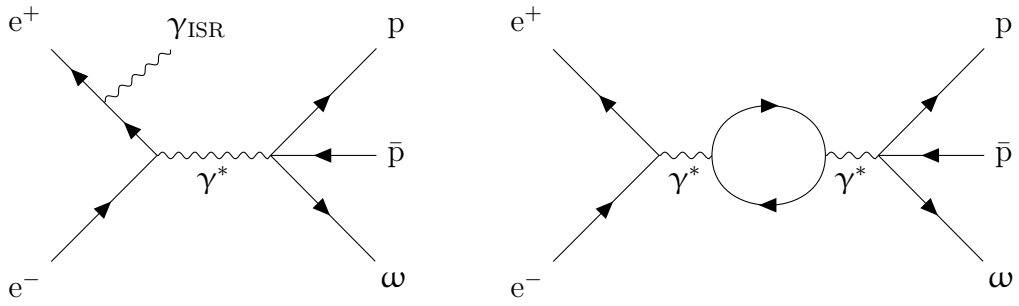

(a) Initial state radiation. **(b)** Vacuum polarization.

Figure 2.7 – Higher order effects contributing to the observed cross section.

2.4 Relativistic kinematic

In particle physics it is useful to use four-vectors to describe the kinematic of a relativistic process. An important quantity is the four-momentum $\mathbb{P}$, which is defined as:

$$\mathbb{P} = \begin{pmatrix} E/c \\ \vec{p} \end{pmatrix} = \begin{pmatrix} E/c \\ p_x \\ p_y \\ p_z \end{pmatrix}. \tag{2.16}$$

Here $\vec{p} = (p_x, p_y, p_z)^{\mathrm{t}}$ is the particle's three-momentum and $E = \sqrt{m_{\mathrm{inv}}^2 c^4 + c^2 \vec{p}^{\,2}}$ is the relativistic energy of the particle. The squared norm of the four-momentum is defined as:

$$\|\mathbb{P}\|^2 = \frac{E^2}{c^2} - \vec{p}^{\,2} = m_{\mathrm{inv}}^2 c^2. \tag{2.17}$$

Since the norm of a four-vector is invariant under Lorentz transformation, the right side of Equation (2.17) has to be Lorentz invariant, too. The quantity m_{inv} is called the invariant or rest mass of the particle [Nol10].
In any reaction, energy and momentum of the particles, i.e. the total four-momentum, is conserved. For a reaction of the kind $\mathrm{a} + \mathrm{b} \to \mathrm{c} + \mathrm{d} + \mathrm{e}$ (like the reaction that is analyzed in this thesis) this means

$$\mathbb{P}_{\mathrm{a}} + \mathbb{P}_{\mathrm{b}} = \mathbb{P}_{\mathrm{c}} + \mathbb{P}_{\mathrm{d}} + \mathbb{P}_{\mathrm{e}}. \tag{2.18}$$

From Equation (2.18) it follows that the mass of a particle (for example particle e) that cannot be detected in an experiment can be determined by:

$$m_{\mathrm{inv,e}} = \frac{1}{c}\|\mathbb{P}_{\mathrm{e}}\| = \frac{1}{c}\|\mathbb{P}_{\mathrm{a}} + \mathbb{P}_{\mathrm{b}} - \mathbb{P}_{\mathrm{c}} - \mathbb{P}_{\mathrm{d}}\|. \tag{2.19}$$

Another case in which this notation can be helpful is when a particle cannot be detected directly, but only via its decay particles (like the ω meson). In the case that the particle decays into three other particles ($\mathrm{e} \to \mathrm{f} + \mathrm{g} + \mathrm{h}$) the decayed particle can be reconstructed from the invariant mass of the system of daughter particles:

$$m_{\mathrm{inv,e}} = \frac{1}{c}\|\mathbb{P}_{\mathrm{e}}\| = \frac{1}{c}\|\mathbb{P}_{\mathrm{f}} + \mathbb{P}_{\mathrm{g}} + \mathbb{P}_{\mathrm{h}}\| =: m_{\mathrm{fgh}}. \tag{2.20}$$

The concept of the invariant mass can also be used in the context of so called Dalitz plots. For a reaction like the one considered in Equation (2.18) the differential cross section $\mathrm{d}\sigma$ can be calculated as [Kho17]

$$\mathrm{d}\sigma = (2\pi)^4 \delta\left(\mathbb{P}_\mathrm{f} - \mathbb{P}_\mathrm{i}\right) \frac{1}{FK} |\mathcal{M}|^2 \frac{\mathrm{d}^3\vec{p}_\mathrm{c}}{(2\pi)^3 2E_\mathrm{c}} \frac{\mathrm{d}^3\vec{p}_\mathrm{d}}{(2\pi)^3 2E_\mathrm{d}} \frac{\mathrm{d}^3\vec{p}_\mathrm{e}}{(2\pi)^3 2E_\mathrm{e}}. \tag{2.21}$$

Here $\delta\left(\mathbb{P}_\mathrm{f} - \mathbb{P}_\mathrm{i}\right)$ with $\mathbb{P}_\mathrm{f} = \mathbb{P}_\mathrm{c} + \mathbb{P}_\mathrm{d} + \mathbb{P}_\mathrm{e}$ and $\mathbb{P}_\mathrm{i} = \mathbb{P}_\mathrm{a} + \mathbb{P}_\mathrm{b}$ is the conservation of four-momentum, $F = 4\sqrt{(\mathbb{P}_\mathrm{a} \cdot \mathbb{P}_\mathrm{b})^2 - m_a^2 m_b^2 c^4}$ is the flux factor, $K = (2s_\mathrm{a} + 1)(2s_\mathrm{b} + 1)$ with s_j being the spin of particle j is the spin multiplicity of the incoming particles and $|\mathcal{M}|^2$ is the transition matrix element. It can be shown (see [Kho17]) that this is equivalent to

$$\mathrm{d}\sigma \sim \mathrm{d}m_{12}^2 \, \mathrm{d}m_{13}^2, \tag{2.22}$$

i.e. the differential cross section is determined by the invariant mass of two of the subsystems of the outgoing particles. In a Dalitz plot the number of events in dependence of the invariant mass of two of the subsystems is shown[3]. If in the reaction intermediate resonances would play a role or there is some kind of final state interaction, one would expect certain structures in the Dalitz plot [Kho17].

[3] Another possibility is a Dalitz plot in dependence of the kinematic energy of the particles.

3 Experimental setup

The datasets that are analyzed in this thesis were collected at the BESIII experiment which is located at the BEPCII (Beijing Electron–Positron Collider II) particle accelerator. BEPCII is a part of the Institute of High Energy Physics (IHEP) in Beijing. In the next sections BEPCII and BESIII will be described.

3.1 BEPCII

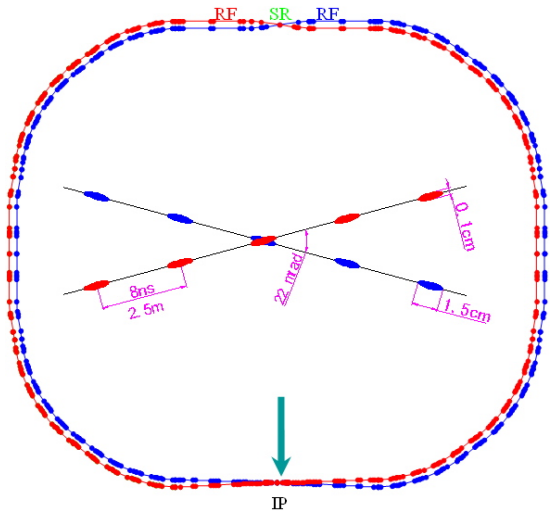

(a) Schematic view of BEPCII [Uni10].

(b) Picture of BEPCII buildings [Ins18].

Figure 3.1 – Left: Schematic view of BEPCII with a zoom into the interaction point (IP), here information on the crossing angle, the bunch spacing and size are listed. The red and blue lines and dots are the beam line for the electron and positron respectively.
Right: A picture of the BEPCII buildings, including the buildings around the storage ring, and the linear pre-accelerator in the top right.

BEPCII, which is an upgrade of BEPC built in the 1980s, is an electron positron collider designed for e^+e^- collisions at center-of-mass energies between 2 and 4.2 GeV

with a design luminosity of $1 \times 10^{33}\,\mathrm{cm}^{-2}\,\mathrm{s}^{-1}$ at $\sqrt{s} = 3.78\,\mathrm{GeV}$ [Har06]. Later, the energy region was expanded up to 4.6 GeV [Zwe09]. This energy region is suitable for experiments to study charm and tau physics, amongst other things.
BEPCII has two beam lines, each with a circumference of 237.5 m. The two lines, one for electrons and one for positrons, depicted in red and blue in Figure 3.1a, cross at the interaction point (IP), at which the BESIII experiment is built, at an angle of 22 mrad. In each line, 93 bunches with a spacing of 8 ns (or 2.5 m) and a length of 1.5 cm circulate simultaneously [A+10]. The design parameters of BEPCII are summarized in Table 3.1.
Electrons and positrons inserted into the storage rings are pre-accelerated in a 202.4 m long linear accelerator up to $E = 1.89\,\mathrm{GeV}$. In addition to its purpose as an electron-positron collider BEPCII can be used as a source for synchrotron radiation. For this purpose several experimental stations have been installed around the collider, where the synchrotron radiation coming from the storage ring can be used in all kind of experiments [Har06].

Table 3.1 – BEPCII design parameters. Excerpt from [A+10].

Center of mass energy $\sqrt{s}$	$2 - 4.6\,\mathrm{GeV}$
Circumference C	$237.5\,\mathrm{m}$
Peak luminosity L	$1 \times 10^{33}\,\mathrm{cm}^{-2}\,\mathrm{s}^{-1}$
Number of bunches N_{bunch}	2×93
Beam current I	$2 \times 0.91\,\mathrm{A}$
Bunch spacing d	$2.5\,\mathrm{m}\ /\ 8\,\mathrm{ns}$
Bunch length σ_z	$1.5\,\mathrm{cm}$
Relative energy spread $\sigma_{E_{\mathrm{beam}}}/E_{\mathrm{beam}}$	5×10^{-4}
Crossing angle α	$22\,\mathrm{mrad}$

3.2 BESIII

The BESIII experiment is an upgrade to the prior existing BES and BESII experiments with new and advanced detector technologies. BES was build for the purpose of τ and charm studies and began operation in 1989. In 1996, it was then upgraded to BESII which was in operation until 2004. The newest update to BESIII, which was completed in 2009, was necessary to account for the significantly higher statistics that was targeted [A+10].

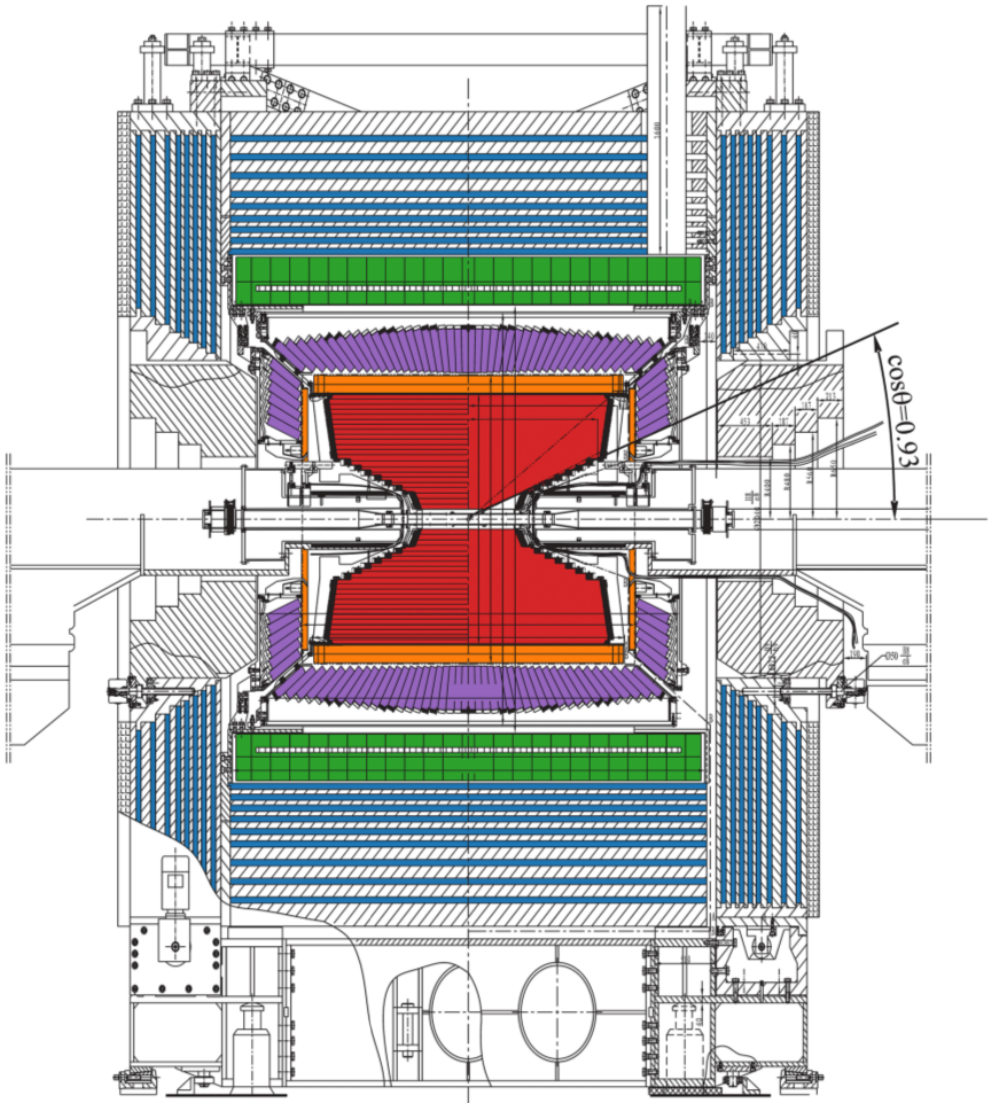

Figure 3.2 – Schematic view of the BESIII experiment with the beams coming from left and right. The different parts of the detector are depicted in colors: The multilayer drift chamber (red), the time-of-flight system (orange), the electromagnetic calorimeter (violet), the superconducting solenoid (green) and the muon identifier (blue). Original picture from [A$^+$10], edited in [Kel17].

The detector consists of several systems of subdetectors with the purpose of particle identification, energy and momentum measurements as well as triggering. These subsystems, which can be seen schematically in Figure 3.2, are: The multilayer drift chamber (MDC), the time-of-flight system (TOF), the electromagnetic calorimeter (EMC) and the muon identifier. Additionally, the detector contains a superconducting solenoid generating a magnetic field inside the detector. A summary of the achieved resolutions as well as some additional parameters for the different parts, which will be described in more detail in the next sections, are displayed in Table 3.2. Here and in the following, the z-axis is the angle bisector of the beam lines with the origin at the interaction point.

Table 3.2 – BESIII detector parameters. Values taken from [A$^+$10, Har06].

MDC	Spatial resolution in $R-\phi$ plane $\sigma_{R-\phi}$	130 µm
	Spatial resolution in z direction σ_z	2 mm
	Momentum resolution σ_p/p at 1 GeV/c	0.5 %
	Energy loss resolution $\sigma_{\mathrm{d}E/\mathrm{d}x}/(\mathrm{d}E/\mathrm{d}x)$	6 %
TOF	Barrel time resolution $\sigma_{t,\mathrm{B}}$	100 ps
	End cap time resolution $\sigma_{t,\mathrm{EC}}$	110 ps
EMC	Energy resolution σ_E/E at 1 GeV	2.5 %
	Spatial resolution σ_r at 1 GeV	6 mm
Muon	Spatial resolution σ_r	16.6 mm
	Cut-off momentum p_{off}	0.4 MeV/c
Solenoid	Magnetic field B	1.0 T

3.2.1 Multilayer drift chamber

The multilayer drift chamber is a detector subsystem designed to determine the momentum of charged particles and to help identifying the particle's type via its specific energy deposit $\frac{\mathrm{d}E}{\mathrm{d}x}$.

A drift chamber is composed of an array of wires at high voltage. The chamber is filled with a gas mixture which in the case of BESIII is 60 % Helium and 40 % propane (C_3H_8) [Har06]. When a charged particle enters the drift chamber it ionizes surrounding atoms or molecules in the gas. The produced ions and electrons are then accelerated towards the wires while ionizing additional atoms or molecules on their way. This results in a cascade which can be seen as charge pulses in the nearest

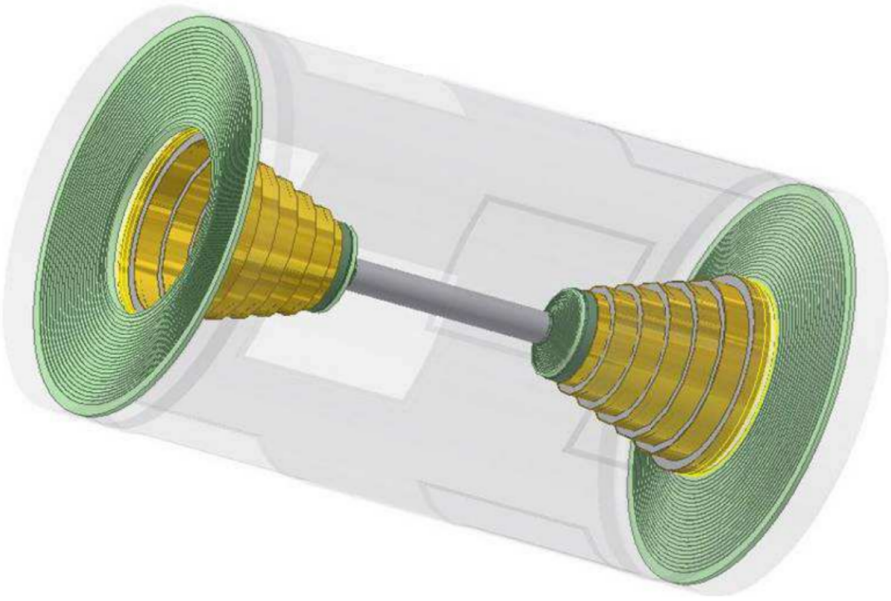

Figure 3.3 – Schematic view of the multilayer drift chamber, with the inner chamber in green, gold and gray and the outer chamber as the transparent cylinder around it [Har06].

wires. As the particle propagates, it produces many of these cascades allowing for a reconstruction of the particle's trajectory. In order to get a good probability to reconstruct the trajectory, multiple layers of drift chambers are used.
In Figure 3.3 the layout of the BESIII multilayer drift chamber is shown, it consists of an inner and an outer chamber with radii of $r_\mathrm{i} = 60\,\mathrm{mm}$ and $r_\mathrm{o} = 800\,\mathrm{mm}$, respectively. The inner chamber is built up from eight and the outer one is built up from thirty-five cylindrical layers of cells with an average half-width of 6 mm and 8.1 mm, respectively. This gives a coverage of the θ angle of: $|\cos\theta| < 0.93$. The spatial resolution of the MDC has been measured to be $\sigma_{R-\phi} = 130\,\mu\mathrm{m}$ in the $R-\phi$ plane and $\sigma_z = 2\,\mathrm{mm}$ in z direction [A$^+$09]. The MDC is placed inside a superconducting solenoid which produces a magnetic field of $B = 1\,\mathrm{T}$. Because of this, the trajectories of charged particles are helices with the helices parameters being dependent on the particles momentum. This allows a calculation of the momentum of the particle at the vertex. Here, a relative resolution of $\sigma_p/p = 0.5\,\%$ at $1\,\mathrm{GeV/c}$ is achieved [A$^+$09].
In addition to the momentum of the particle, the energy deposit per distance $\frac{\mathrm{d}E}{\mathrm{d}x}$ can be determined from the intensity of the charge pulses in the wires. For the BESIII MDC a resolution of $\frac{\sigma_{\mathrm{d}E/\mathrm{d}x}}{\mathrm{d}E/\mathrm{d}x} = 6\,\%$ has been measured [A$^+$09].

3.2.2 Time-of-flight system

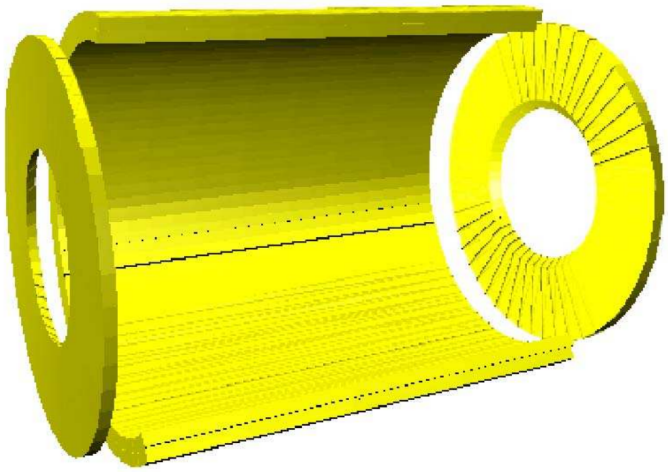

Figure 3.4 – Schematic view of the time-of-flight system, with the barrel built up of two layers of eighty-eight staggered scintillating bars each and the two end caps built up of forty-eight fan-shaped scintillators [Har06].

With the time-of-flight system information about charged particles are gathered. These information can be used for the purpose of particle identification. Additionally, the TOF system can be used as a trigger.
The TOF system consists of three parts: The barrel and the two end caps (as shown in Figure 3.4). The barrel is built up from two times eighty-eight plastic scintillators arranged in two layers at a mean radius of $\bar{r} = 870\,\mathrm{mm}$ and each end cap is composed of forty-eight fan-shaped scintillators with an inner radius of $r_\mathrm{i} = 410\,\mathrm{mm}$ and an outer radius of $r_\mathrm{o} = 890\,\mathrm{mm}$. Readout of the scintillators is performed via photomultipliers mounted on both ends of each element. With the geometry of the elements used in the TOF a coverage of the θ angle of $|\cos\theta| < 0.83$ for the barrel and $0.85 < |\cos\theta| < 0.95$ for the end cap is achieved. For the time resolution values of $\sigma_{t,\mathrm{B}} = 100\,\mathrm{ps}$ for the barrel and $\sigma_{t,\mathrm{EC}} = 110\,\mathrm{ps}$ for the end cap have been determined [A$^+$10].

3.2.3 Electromagnetic calorimeter

In the BESIII electromagnetic calorimeter the energy and position of electrons and photons is measured. This gives additional information on the four momentum of electrons which is also measured by the MDC. For photons the four momentum can be

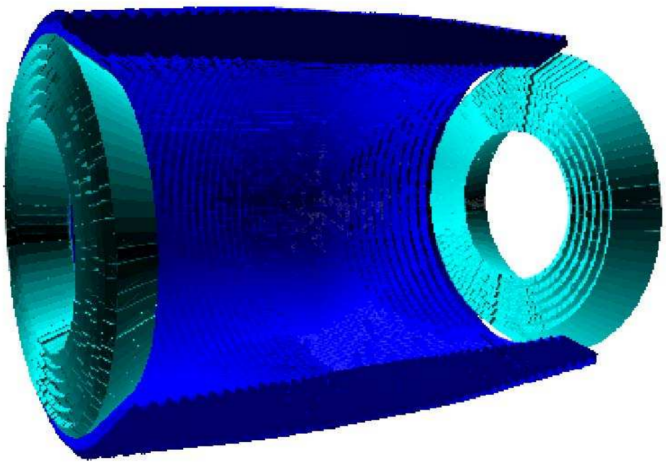

Figure 3.5 – Schematic view of the electromagnetic calorimeter, with the barrel part in blue and the enc caps in turquoise [Har06].

completely calculated from the angles and the deposited energy in the electromagnetic calorimeter.

The BESIII EMC consists of 6272 thallium-doped cesium iodide crystals formed as truncated square pyramids with a side length of 5 cm on the front face, 6.5 cm on the rear face and a length of 28 cm (15 radiation lengths). They are divided into the barrel part and two endcaps with the crystals pointing towards the interaction point, as can be seen in Figure 3.5. The inner radius of the barrel part is $r_{\mathrm{i,B}} = 940\,\mathrm{mm}$ with a total length of $l_z = 2750\,\mathrm{mm}$ and the inner radius of the end caps is $r_{\mathrm{i,EC}} = 500\,\mathrm{mm}$ at a position of $z = \pm 1380\,\mathrm{mm}$. This leads to an angular coverage for the barrel of $|\cos\theta| < 0.83$ and of $0.85 < |\cos\theta| < 0.93$ for the end caps. The spatial resolution is 6 mm at $E_\gamma = 1\,\mathrm{GeV}$ [Har06].

When an electron or a photon enters such a crystal they produce an electromagnetic shower via bremsstrahlung and e^+e^--pair production and therefore deposit their energy in the crystals. These function as scintillators and the produced light is measured via photodiodes. The energy can then be calculated from the light yield with a relative resolution of 2.5 % at $E_\gamma = 1\,\mathrm{GeV}$ [A$^+$10].

3.2.4 Muon identifier

As the outermost part of BESIII, the muon identifier system is installed inside an iron return yoke. This system's main purpose is the distinction of muons and hadrons

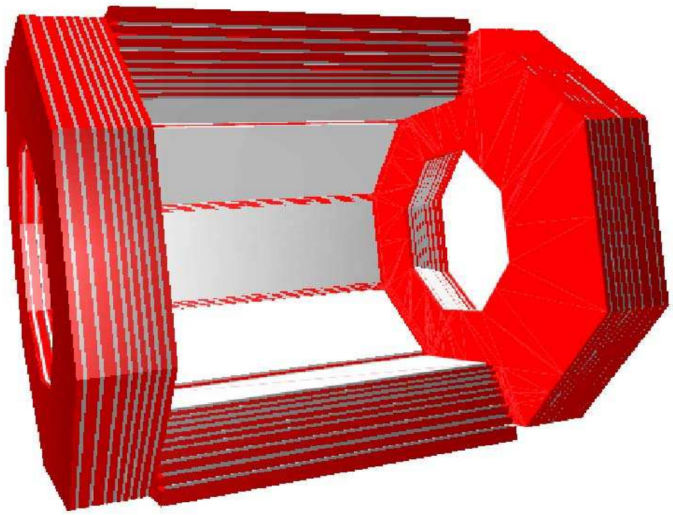

Figure 3.6 – Schematic view of the muon identifier with the iron absorbers in red and the resistive plate chambers in gray [Har06].

(mostly pions) by their hit pattern in the yoke which has the purpose of containing the magnetic field. Electrons and positrons, as well as strongly interacting particles like pions cannot penetrate the iron and give therefore a different signature in the layers.

Again, this subdetector is divided into a barrel part and two end caps. As can be seen in Figure 3.6, the barrel part consists of nine layers of resistive plate chambers (RPCs) and the end caps consist of eight layers of RPCs, each with a thickness of 4 cm. The single layers are separated by iron with increasing thickness: First three layers with $d = 3\,\text{cm}$, then two layers with $d = 4\,\text{cm}$, followed by three layers with $d = 8\,\text{cm}$ and a last layer with $d = 15\,\text{cm}$).

A resistive plate chamber is a particle detector similar to the drift chambers where the incoming charged particles ionize a gas mixture inside a volume that is enclosed by electrodes under high voltage. The ionized molecules and the electrons produce a cascade and can be measured as a charge pulse in the electrodes. Due to a segmentation of the electrodes a spatial information of the detected particles can be obtained, which for BESIII gives a resolution of $\sigma_r = 16.6\,\text{mm}$.

Since the muons already loose energy in the inner detector parts there is a cut-off momentum under which the muons cannot reach the identifier system and can therefore not be detected. This cut-off is at $p_{\text{off}} = 0.4\,\text{MeV/c}$.

3.3 Datasets

The datasets analyzed in this thesis have been taken at the BESIII experiment in the period between 2011 and 2017 for the purpose of XYZ studies. The center-of-mass energies and the integrated luminosities are listed in Table 3.3. Since at the end an energy dependent cross section will be calculated, only datasets with $L_{\text{int}} > 100\,\text{pb}^{-1}$ are used, because in smaller datasets the expected statistics would be too small for the chosen analysis strategy.

Table 3.3 – Datasets used in this analysis with their center-of-mass energy and integrated luminosity.

Dataset	Center-of-mass energy $\sqrt{s}$/MeV	Integrated luminosity $L_{\text{int}}/\text{pb}^{-1}$
4040	4007.6 ± 0.8	482.0 ± 4.8
4180	4178.4 ± 0.8	3161.0 ± 31.8
4190	4188.8 ± 0.8	522.5 ± 3.4
4200	4198.9 ± 0.8	524.6 ± 2.5
4210	4209.2 ± 0.8	518.1 ± 1.8
4220	4218.7 ± 0.8	514.3 ± 1.9
4230	4226.3 ± 0.7	1056.4 ± 7.1
4237	4235.7 ± 0.8	530.6 ± 2.4
4246	4243.8 ± 0.8	537.4 ± 2.6
4260	4258.0 ± 0.7	828.4 ± 5.6
4270	4266.8 ± 0.8	529.7 ± 2.8
4280	4277.7 ± 0.8	175.5 ± 0.9
4360	4358.3 ± 0.7	543.9 ± 3.7
4420	4415.6 ± 0.7	1043.9 ± 7.1
4600	4599.5 ± 0.8	586.9 ± 4.0

In addition, for each of these center-of-mass energies a Monte Carlo generator was used to create a simulation of 550 000 signal events. The events were created using the generators KKMC and BesEvtGen. KKMC is a generator for processes of the type $\text{e}^+\text{e}^- \to f\bar{f} + n \cdot \gamma$ with $f = \mu, \tau, \text{u}, \text{d}, \text{s}, \text{c}, \text{b}$ at energies from

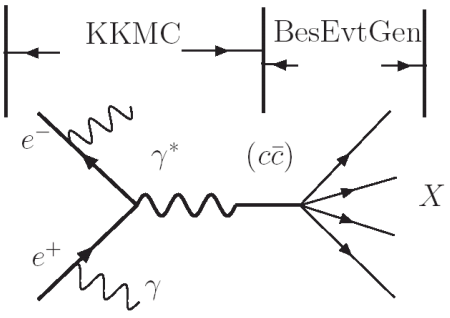

Figure 3.7 – Schematic diagram of the process $e^+e^- \to X$ generated with KKMC and BesEvtGen. The left part including the electron and positron propagation, initial state radiation, as well as the production of a $c\bar{c}$-state through a virtual photon are generated with KKMC. The right part including the subsequent decay of the $c\bar{c}$-state into multiple particles is generated with BesEvtGen [Pin08].

$E = 2m_\tau c^2 = (3553.72 \pm 0.24)\,\mathrm{MeV}$ [T+18] to $E = 1\,\mathrm{TeV}$ [JWW00]. The decays of produced charmonium states are then modeled by the generator BesEvtGen [PP07]. This is shown schematically in Figure 3.7. BesEvtGen is based on the Generator EvtGen which was originally designed for the study of B physics [R+07]. In BesEvtGen any possible decay chain of a charmonium state can be generated with a variety of different models. For this thesis, the decay chain is

$$\begin{aligned} e^+e^- &\to p\bar{p}\omega, \\ \omega &\to \pi^+\pi^-\pi^0, \\ \pi^0 &\to \gamma\gamma, \end{aligned} \tag{3.1}$$

with all decays being evenly distributed in phase space. The events that are created with KKMC and BesEvtGen are then processed by the detector simulation software GEANT4 [A+03] to generate a simulation file that can be handled similar to real data, but that also contains information on the generated values for momentum and energy of the particles.

To perform studies on possible background reactions an inclusive Monte Carlo sample at $\sqrt{s} = (4178.4 \pm 0.8)\,\mathrm{MeV}$ is used. In this sample all known possible reactions at that energy are simulated with their measured cross sections. For reactions where no cross section has been measured yet, it is estimated according to the Lund model [AH99] with the program LUARLW [HT01].

4 Analysis

In this chapter, the analysis steps that were performed are presented, starting with the basic event selection, followed by cuts used for background reduction. After that, results for invariant mass spectra, Dalitz plots, efficiency and ISR correction are shown. Finally, the Born cross section for the reaction $e^+e^- \to p\bar{p}\omega$ and an upper limit on the Born cross section for the process $e^+e^- \to Y \to p\bar{p}\omega$ are presented.

4.1 Basic event selection

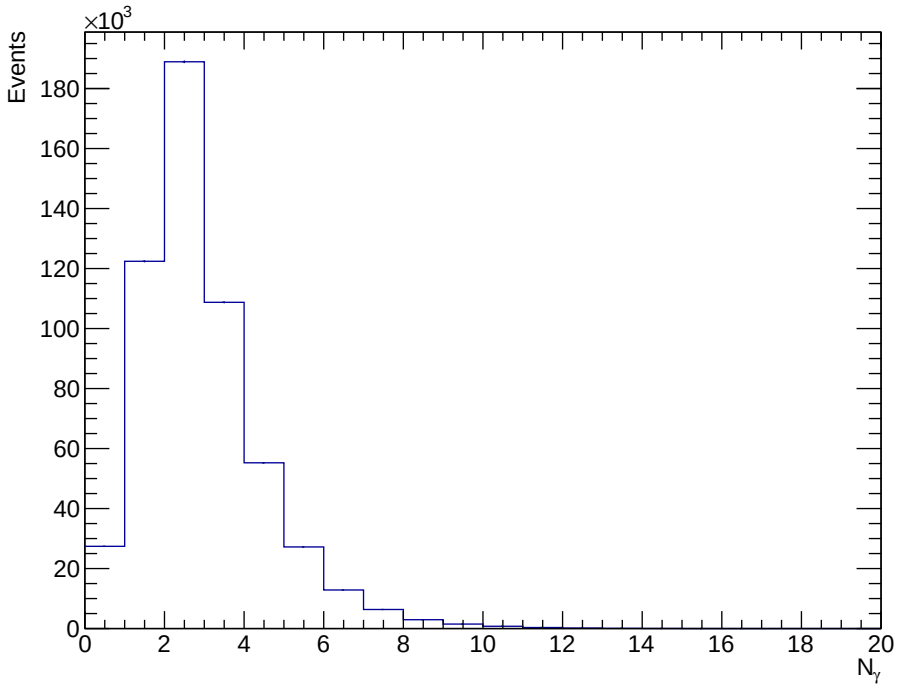

Figure 4.1 – Number of accepted photons for a simulation of the reaction $e^+e^- \to p\bar{p}\omega$.

Each event that is considered in the analysis has to fulfill the signature

$$e^+e^- \to p\bar{p}\pi^+\pi^-\gamma\gamma. \tag{4.1}$$

This is achieved by demanding exactly one good proton, antiproton, π^+ and π^- track in the event. In order to get a better efficiency, the number of good photons does not need to be exactly two, but has to be at least two. The reason for this is that often additional photons are produced in the interaction of particles with the detector. An example can be seen in Figure 4.1, where the number of accepted photons in a simulation of $e^+e^- \to p\bar{p}\omega$ is displayed. It is seen, that the number of photons has a maximum at two, but extends to higher numbers, even if only the two photons from the π^0 decay and potentially ISR photons were generated.
In order for a track to be considered a good track it has to fulfill various conditions. On the one hand, a vertex cut is used which means that a track has to have a point of closest approach to the interaction point (the vertex) inside a cylindrical volume around the interaction point. This is achieved by requiring the vertex coordinates to be $V_r = \sqrt{V_x^2 + V_y^2} < 1\,\text{cm}$ and $|V_z| < 10\,\text{cm}$. On the other hand, the geometric constraints of the detector have to be satisfied: For a charged track the polar angle in the MDC is constrained by $|\cos\theta| < 0.93$ and for a photon the polar angle in the EMC is constrained by $|\cos\theta| < 0.8$ or $0.86 < |\cos\theta| < 0.92$. For photons some additional conditions have to be fulfilled: A minimum energy deposit in the EMC of $E_{\text{min,B}} = 25\,\text{MeV}$ in the barrel and $E_{\text{min,EC}} = 50\,\text{MeV}$ in the end cap, a timing cut of $t_{\text{EMC}} < 700\,\text{ns}$ and a cut on the angle between the photon and next proton/antiproton of $\sphericalangle(p/\bar{p}, \gamma) > 10°/30°$. The larger angle with respect to the antiproton track is accounts for the large showers originating from antiproton annihilation inside the calorimeter.
To determine the type of a track, the BESIII particle identification system is utilized which can use information from all parts of the detector to calculate a probability for a track to be a proton, pion, kaon, etc. These probabilities are compared and then used to assign the track's type.
A summary of the basic event selection criteria can be found in Table 4.1.

Table 4.1 – Summary of the basic event selection criteria used in the analysis.

Event	Number of good $\mathrm{p}/\bar{\mathrm{p}}$ tracks	$N_{\mathrm{p}}/N_{\bar{\mathrm{p}}} = 1$
	Number of good π^+/π^- tracks	$N_{\pi^+}/N_{\pi^-} = 1$
	Number of good γ tracks	$N_\gamma \geq 2$
Charged tracks	Vertex cut	$V_r < 1\,\mathrm{cm}$
		$\lvert V_z\rvert < 10\,\mathrm{cm}$
	Polar angle cut	$\lvert\cos\theta\rvert < 0.93$
Photons	Minimum energy deposit	$E_{\mathrm{B}} > 25\,\mathrm{MeV}$
		$E_{\mathrm{EC}} > 50\,\mathrm{MeV}$
	Polar angle cut	$\lvert\cos\theta_{\mathrm{B}}\rvert < 0.8$
		$0.86 < \lvert\cos\theta_{\mathrm{EC}}\rvert < 0.92$
	Timing cut	$t_{\mathrm{EMC}} < 700\,\mathrm{ns}$
	Angle to next $\mathrm{p}/\bar{\mathrm{p}}$	$\sphericalangle(\mathrm{p},\gamma) > 10^\circ$
		$\sphericalangle(\bar{\mathrm{p}},\gamma) > 30^\circ$

4.2 Kinematic fit and background subtraction

In order to get the two γ's that form the best π^0 candidate a kinematic fit of the tracks and γ showers to the hypothesis

$$h_1 : \ \mathrm{e^+e^-} \to \mathrm{p\bar{p}}\pi^+\pi^-\pi^0, \quad \pi^0 \to \gamma\gamma \tag{4.2}$$

is applied. In a kinematic fit the measured momenta of the particles are altered to get compliance with conservation of four-momentum (four constraints), which may not be satisfied due to uncertainties of the detector in the measurement. In this case, an additional constraint on the invariant mass of the π^0 candidate is added to the kinematic fit. It is required to be exactly the mass of the π^0. So in total there are five constraints (5C). The fit is done for every possible combination of two photons and the one that yields the best χ^2 is kept as the π^0.
The invariant mass spectrum of the three pions that form the ω for the dataset at $\sqrt{s} = (4178.4 \pm 0.8)\,\mathrm{MeV}$ after the kinematic fit can be seen in Figure 4.2. A peak around the ω mass above a continuous background can be seen. To subtract the background contribution a quadratic fit of the form

$$f(m_{\pi^+\pi^-\pi^0}) = a + b \cdot m_{\pi^+\pi^-\pi^0} + c \cdot m^2_{\pi^+\pi^-\pi^0} \tag{4.3}$$

is applied to the data excluding the peak region ($720\,\mathrm{MeV/c^2} < m_{\pi^+\pi^-\pi^0} < 850\,\mathrm{MeV/c^2}$) which gives

$$\begin{aligned} a &= (42.8 \pm 5.6)\frac{\text{Events}}{2.5\mathrm{MeV/c^2}}, \\ b &= (-0.174 \pm 0.014)\frac{\text{Events}}{2.5(\mathrm{MeV/c^2})^2}, \\ c &= (1.81 \pm 0.08) \times 10^{-4}\frac{\text{Events}}{2.5(\mathrm{MeV/c^2})^3}. \end{aligned} \tag{4.4}$$

The spectra including the background fits for the other datasets can be found in Appendix A.1. The subtracted spectra are later used to calculate the number of observed events (see Section 4.5).

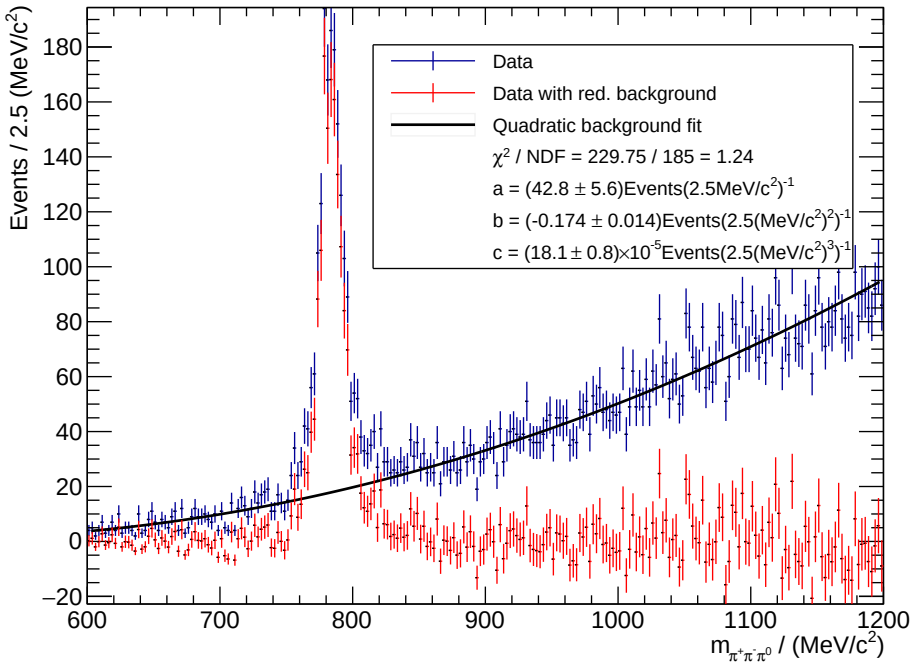

Figure 4.2 – Invariant mass spectrum of the three pions after the kinematic fit. A quadratic fit excluding the peak region is performed to subtract the background.

A possibility to investigate on any potential background surviving the kinematic fit, is the usage of the inclusive Monte Carlo sample. With this sample it is possible to see whether an event passing the kinematic fits is a signal or a background event. This can be seen in Figure 4.3 where the invariant mass of the three pions is shown

for data and for the inclusive Monte Carlo set. Here, additionally the background contributions are highlighted. After scaling the signal contribution and the background contribution to the integral of the corresponding contribution in data they show reasonable compliance.

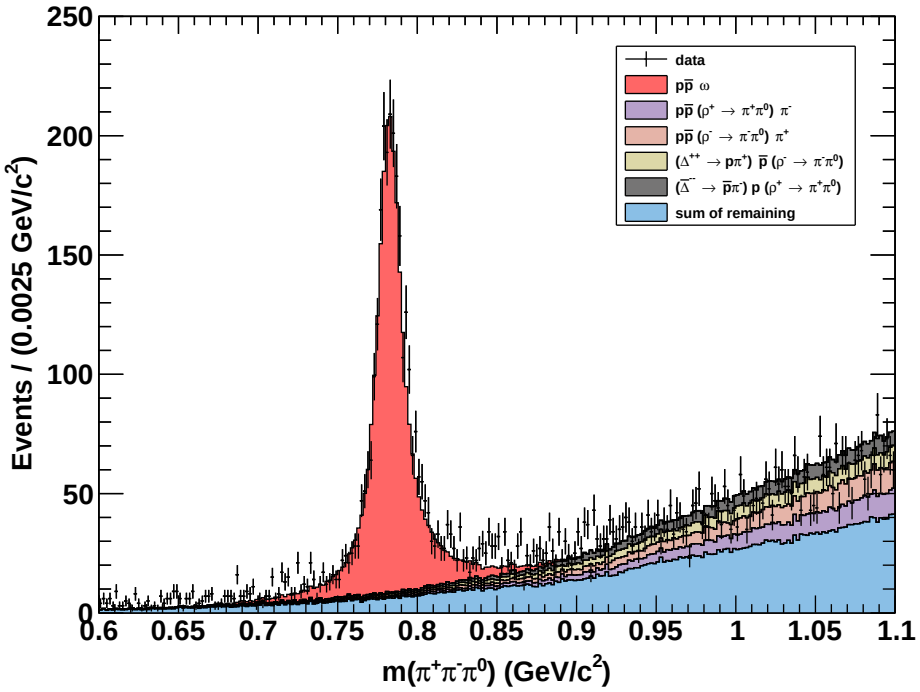

Figure 4.3 – Invariant mass of the three pions after the kinematic fit. In black the data is shown. The contributing reactions determined with the scaled inclusive Monte Carlo sample are depicted in colors.

Now a cut on the χ^2 of the kinematic fit with the hypothesis h_1 is imposed and for different values of χ^2_{cut} a figure of merit is calculated, which can be seen in Figure 4.4. Here the χ^2 distribution for data, for the inclusive MC sample and the corresponding background contribution are shown. These are used to calculate the figure of merit (FOM) which is defined to be

$$\text{FOM} = \frac{S}{\sqrt{S+B}}, \tag{4.5}$$

with S being the number of signal events and B being the number of background

events surviving the χ^2 cut. The reason for this definition of the FOM is the wanted maximization of the significance of the signal above the background. In the resulting plot no maximum can be observed which means that no improvement of the significance of the signal can be achieved by introducing a cut on the χ^2. Consequently no cut, apart from convergence, is applied. Only the fitted values for the momenta are kept.

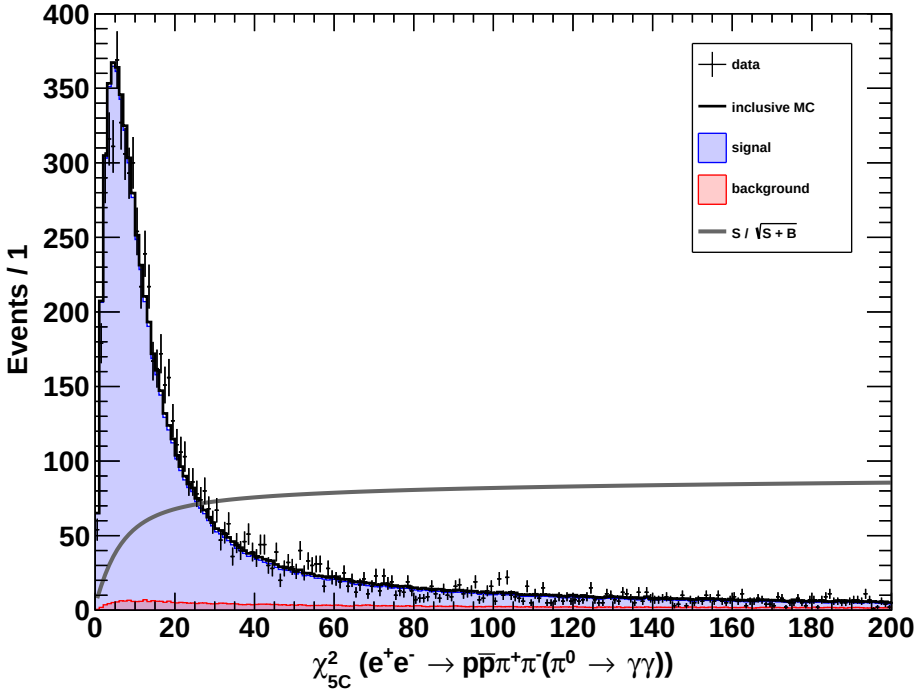

Figure 4.4 – χ^2 distribution for data (black) and for the inclusive MC sample (blue). The background contribution is highlighted in red. Additionally the figure of merit for different values of the χ^2-cut is shown.

4.3 Examination of subsystems

After the initial event selection and the kinematic fit, the reconstructed four-momenta can be used to fill Dalitz plots with the invariant masses of the subsystems $p\bar{p}$, $p\omega$ and $\bar{p}\omega$ of the three final state particles. Assuming the ω couples equally to the proton and antiproton, the invariant mass of the $p\omega$ system and the $\bar{p}\omega$ system are filled in the same histogram. To eliminate contributions stemming from background reactions the plots are filled on the one hand side for the signal region which is defined to be $740\,\mathrm{MeV/c^2} < m_{\pi^+\pi^-\pi^0} < 820\,\mathrm{MeV/c^2}$ and on the other hand for the two sideband regions $620\,\mathrm{MeV/c^2} < m_{\pi^+\pi^-\pi^0} < 700\,\mathrm{MeV/c^2}$ and $860\,\mathrm{MeV/c^2} < m_{\pi^+\pi^-\pi^0} < 940\,\mathrm{MeV/c^2}$. With the assumption that the background behaves equally in these regions the background contributions can be subtracted from the Dalitz plot by subtracting the corresponding sideband plots weighted by a factor of 0.5. The corrected Dalitz plot with $m^2_{p\omega}$ and $m^2_{\bar{p}\omega}$ plotted against $m^2_{p\bar{p}}$ is shown in Figure 4.5 for data and signal MC from the dataset at $\sqrt{s} = (4178.4 \pm 0.8)\,\mathrm{MeV}$. The corresponding Dalitz plots for data from the other datasets can be found in Appendix A.2. In the Dalitz plots for data an enhancement at small invariant masses of the $p\bar{p}$-subsystem can be seen in all datsets. The Dalitz plot for the signal MC events is flat, which was to be expected, since the events were generated evenly distributed in phase space.
In Figure 4.6 the corrected Dalitz plot in dependence of $m^2_{p\omega}$ and $m^2_{\bar{p}\omega}$ is shown for the dataset at $\sqrt{s} = (4178.4 \pm 0.8)\,\mathrm{MeV}$. The plots for the other datasets are displayed in Appendix A.3. In the plots an enhancement on a diagonal line on the top right can be seen, which corresponds to the enhancement seen in Figure 4.5. Again the Dalitz plot for signal MC is flat. This means that the efficiency of the analysis and the acceptance of the detector do not depend on the invariant masses of the particles and are therefore just a function of the center-of-mass energy of the dataset.
Another possibility to investigate the different subsystems of the final state is the consideration of events in dependence of just one of the invariant masses of the subsystems. This corresponds to projections of the Dalitz plots in Figures 4.5 and 4.6 onto the ordinate and abscissa. For the dataset at $\sqrt{s} = (4178.4 \pm 0.8)\,\mathrm{MeV}$ these spectra are presented in Figure 4.7. The spectra for the other datasets can be found in Appendices A.4 and A.5. Here, again, the enhancement at low $p\bar{p}$ invariant masses can be seen. These low masses correspond to a small relative motion between the proton

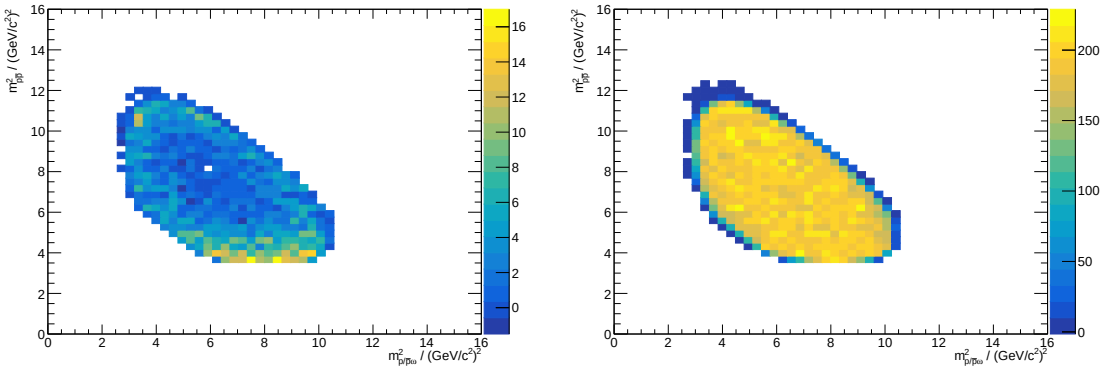

(a) Data. **(b)** Signal MC.

Figure 4.5 – Dalitz plot with the squared invariant masses $m^2_{\mathrm{p}\omega}$ and $m^2_{\bar{\mathrm{p}}\omega}$ plotted against $m^2_{\mathrm{p}\bar{\mathrm{p}}}$ for data and signal MC from the dataset at $\sqrt{s} = (4178.4 \pm 0.8)\,\mathrm{MeV}$. Each event corresponds to two entries since $m_{\mathrm{p}\omega}$ and $m_{\bar{\mathrm{p}}\omega}$ are filled in the same histogram.

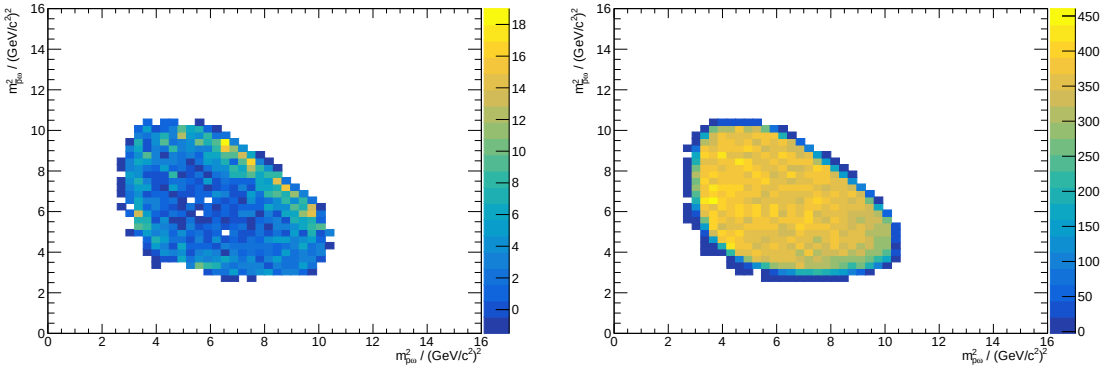

(a) Data. **(b)** Signal MC.

Figure 4.6 – Dalitz plot with the squared invariant masses $m^2_{\mathrm{p}\omega}$ plotted against $m^2_{\bar{\mathrm{p}}\omega}$ for data and signal MC from the dataset 4180.

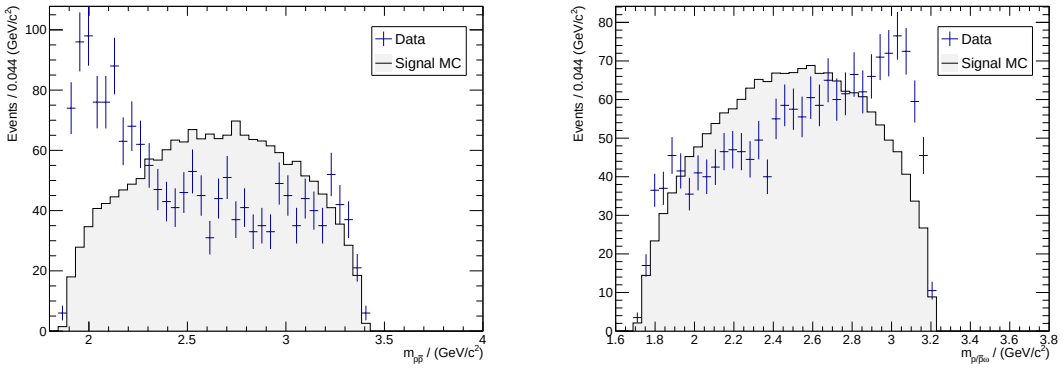

(a) $p\bar{p}$-subsystem. **(b)** $p/\bar{p}\omega$-subsystem.

Figure 4.7 – Invariant mass spectrum of the $p\bar{p}$-subsystem (left) and the $p/\bar{p}\omega$-subsystem (right) for the 4180 dataset.

and antiproton where final state interaction might play a role. Another possible explanation for this enhancement is the contribution of the possibly exotic particle X(1835) that has been seen by the BES collaboration in the decay $J/\psi \to \gamma p\bar{p}$ [B$^+$03] and was later also seen in other decays like $J/\psi \to \gamma\pi^+\pi^-\eta'$ [A$^+$05a]. It has a mass of $M_{X(1835)} = 1826.5^{+13.0}_{-3.4}\,\text{MeV}$ [T$^+$18] and a width of $\Gamma_{X(1835)} = 242^{+14}_{-15}\,\text{MeV}$ [T$^+$18]. In the spectrum of the $p/\bar{p}\omega$ subsystem an ascent towards higher invariant masses can be seen which has its origin in the structure that can be seen in the $p\bar{p}$ invariant masses. To get a better view of possible contributions of intermediate resonances the invariant mass spectra are also filled for the sum of all datasets which can be seen in Figure 4.8. For the structure of the $p/\bar{p}\omega$ invariant mass spectrum many different nucleon resonances N* could play a role. The ones with the biggest branching ratio for the decay into $p/\bar{p}\omega$ are the N(1895) with a branching ratio of $\text{BR}(N^* \to N\omega) = (28 \pm 12)\,\%$, a mass of $M_{N(1895)} = (1895 \pm 25)\,\text{MeV}$ and a width of $\Gamma_{N(1895)} = (120 \pm 40)\,\text{MeV}$, as well as the the N(2100) with a branching ratio of $\text{BR}(N^* \to N\omega) = (15 \pm 10)\,\%$, a mass of $M_{N(2100)} = (2100 \pm 50)\,\text{MeV}$ and a width of $\Gamma_{N(2100)} = (260 \pm 60)\,\text{MeV}$ [T$^+$18]. Because of their huge width and their corresponding overlap it is difficult to exactly identify these peaks. For a deeper analysis of these spectra, a partial wave analysis (PWA) would be necessary.

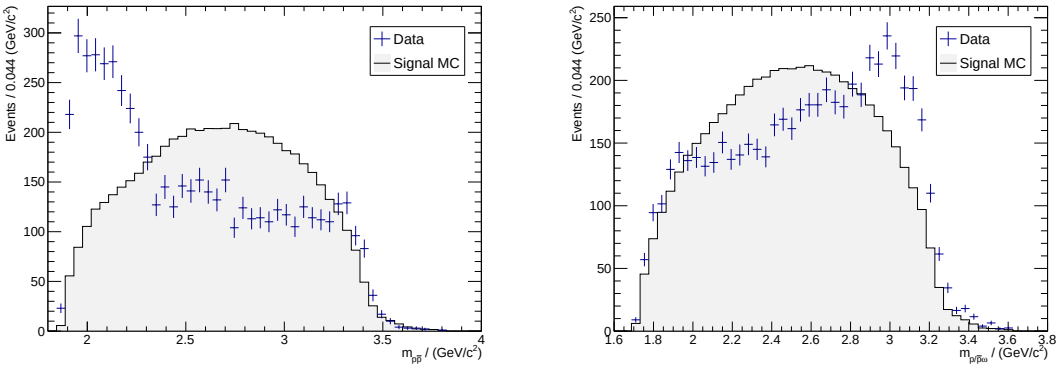

(a) $\mathrm{p\bar{p}}$-subsystem. **(b)** $\mathrm{p}/\bar{\mathrm{p}}\omega$-subsystem.

Figure 4.8 – Invariant mass spectrum of the $\mathrm{p\bar{p}}$-subsystem (left) and the $\mathrm{p}/\bar{\mathrm{p}}\omega$-subsystem (right) for the sum over all datasets.

4.4 Determination of efficiency and ISR correction

The ISR correction factor $(1+\delta_\mathrm{r})$, needed to calculate the Born cross section from the measured cross section (see Equation (2.13)), is determined with the event generator KKMC. The correction factor depends on the center-of-mass energy $\sqrt{s}$ and also on the behavior of the Born cross section $\sigma_\mathrm{Born}(\sqrt{s})$. Because of this, the correction factor is determined iteratively. For the zeroth iteration, a constant cross section is used. The resulting correction factors are then used to calculate the Born cross section which than is fed again into the generator. This is repeated until the radiation correction factors converge. In Figure 4.9, the correction factor after the first, second and third iteration is shown. Since the relative deviation from the third to the fourth iteration is negligible and lies within the uncertainty of the third iteration, the third iteration is kept as the final value for the correction factor.
To determine the efficiency $\varepsilon = \frac{N_\mathrm{rec}}{N_\mathrm{gen}}$ the signal MC samples are used. For each center-of-mass energy the number of reconstructed events N_rec is determined via a fit to the invariant mass spectrum of the three pions.

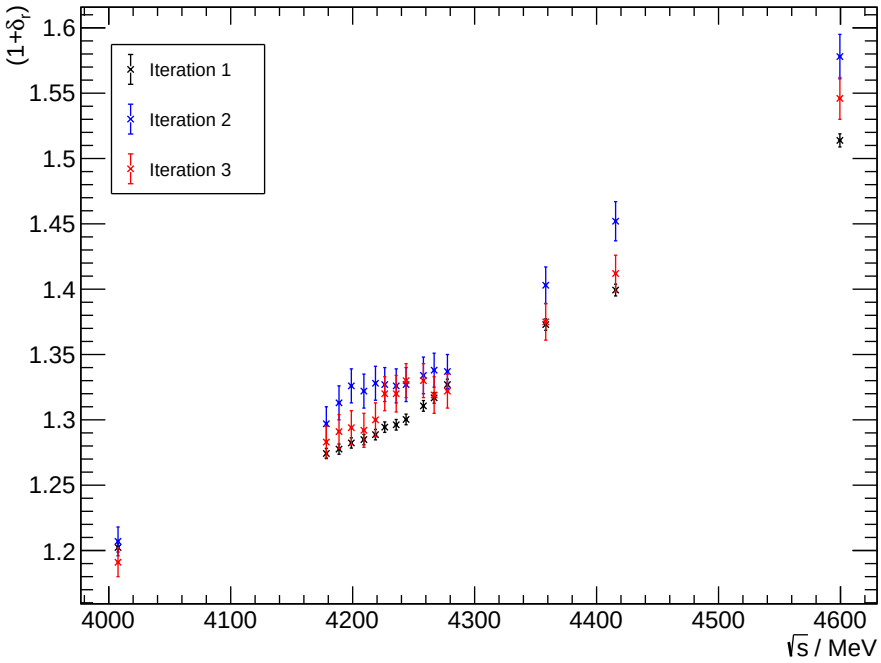

Figure 4.9 – Radiation correction factor $(1 + \delta_r)$ in dependence of the center-of-mass energy $\sqrt{s}$ for the different iterations.

For the fit a Voigt profile $V(m_{\pi^+\pi^-\pi^0})$, which is a convolution of a normalized Breit-Wigner distribution $L(m_{\pi^+\pi^-\pi^0})$ and a Gaussian $G(m_{\pi^+\pi^-\pi^0})$, is used to describe the spectrum. It is defined as

$$\begin{aligned} V(m_{\pi^+\pi^-\pi^0}) &= I \int_{-\infty}^{\infty} G(m')L(m_{\pi^+\pi^-\pi^0} - m')\,\mathrm{d}m' \qquad (4.6)\\ &= I \int_{-\infty}^{\infty} \left[\frac{1}{\sqrt{2\pi\sigma^2}} \exp\left(-\frac{m'^2}{2\sigma^2}\right)\right] \left[\frac{\Gamma}{2\pi} \frac{1}{(m_{\pi^+\pi^-\pi^0} - m_0 - m')^2 + \Gamma^2}\right] \mathrm{d}m'. \end{aligned}$$

Here I is a scaling factor, m_0 is the position of the peak, Γ is the full width at half maximum of the Breit-Wigner distribution and σ is the standard deviation of the Gaussian. The Voigt profile is used to account for the resolvable width of the ω of $\Gamma = (8.49 \pm 0.08)\,\mathrm{MeV/c^2}$ [T+18], which was fixed to the PDG central value in the fit, and the nearly Gaussian-like smearing of the detector which should be of the same order of magnitude.

In Figure 4.10 the Voigt fit for the MC sample at $\sqrt{s} = (4178.4 \pm 0.8)\,\mathrm{MeV}$ is shown. The fitted values for the parameters are

$$\begin{aligned} I &= (7.79 \pm 0.03) \times 10^4 \frac{\mathrm{Events}}{\mathrm{MeV/c^2}}, \\ m_0 &= (782.83 \pm 0.04)\,\mathrm{MeV/c^2}, \\ \sigma &= (5.44 \pm 0.05)\,\mathrm{MeV/c^2}, \\ \chi^2/\mathrm{NDF} &= 914.1/87 = 10.51. \end{aligned} \tag{4.7}$$

The huge χ^2_{red} is produced by a slight asymmetry of the peak, which can not be described by the chosen profile. To get the number of reconstructed events from this a symmetric interval around the peak is determined containing 95 % of the area of the whole peak. The fitted function is then integrated in this interval and divided by the number of generated events to get the efficiency. The difference between the fit model and the spectrum has only a negligible effect.
The calculated efficiencies for all datasets are presented in Figure 4.11. It can be seen that the efficiency decreases towards higher center-of-mass energies. This can be explained partly by the fact that the ISR correction factor increases towards higher energies so the efficiency gets reduced. Because of this dependency the more meaningful quantity, is the product of the ISR correction factor and efficiency, which is also plotted in Figure 4.11. For the product the slope is much lower as for the efficiency, however, in both cases there are outliers at the 4040, 4230, 4360 datasets and a small one at the 4260 dataset. These sets were taken before 2014 while the others were taken after 2014. This is an effect produced by changes to the reconstruction algorithm of tracks.

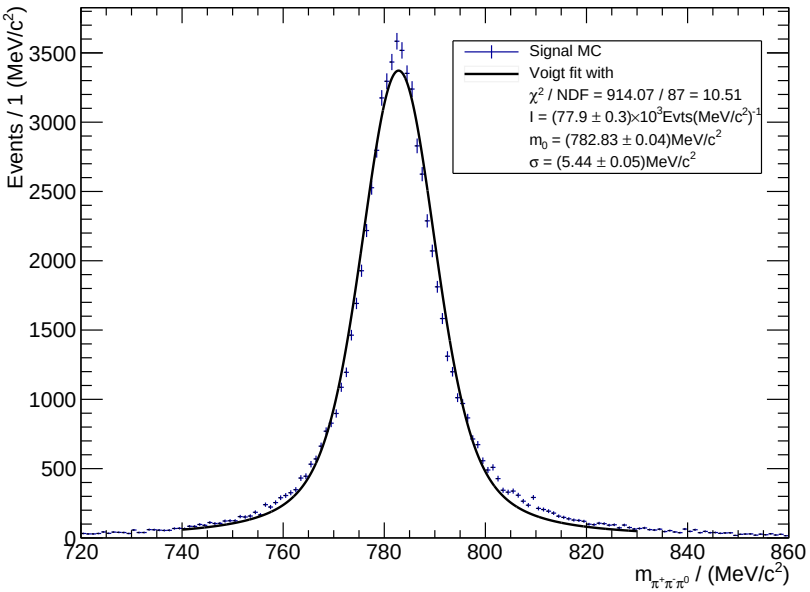

Figure 4.10 – Voigt fit to the invariant mass spectrum of the three pions for the signal MC sample at $\sqrt{s} = (4178.4 \pm 0.8)\,\mathrm{MeV}$.

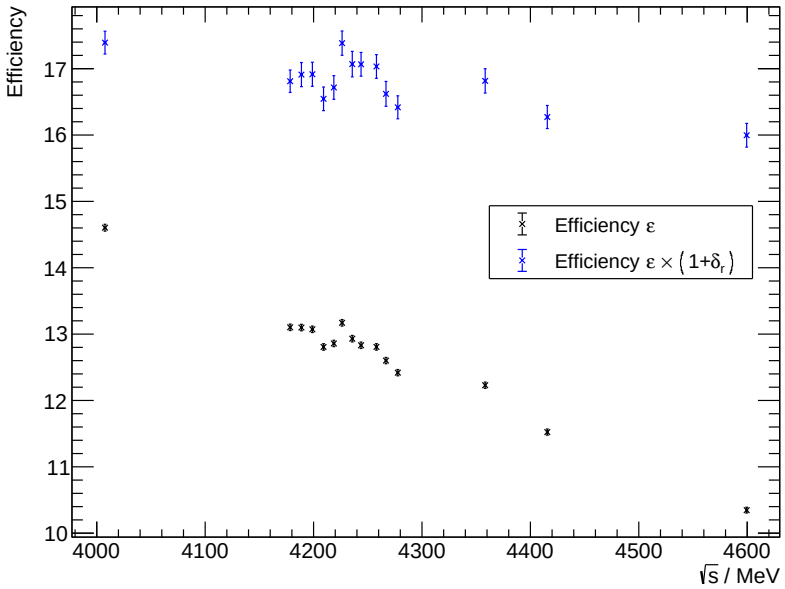

Figure 4.11 – Efficiency ε of the analysis including the geometrical acceptance of the detector in dependence of the center-of-mass energy. Additionally, the product of efficiency and ISR correction factor is shown.

4.5 Determination of the Born cross section for $e^+e^- \to p\bar{p}\omega$

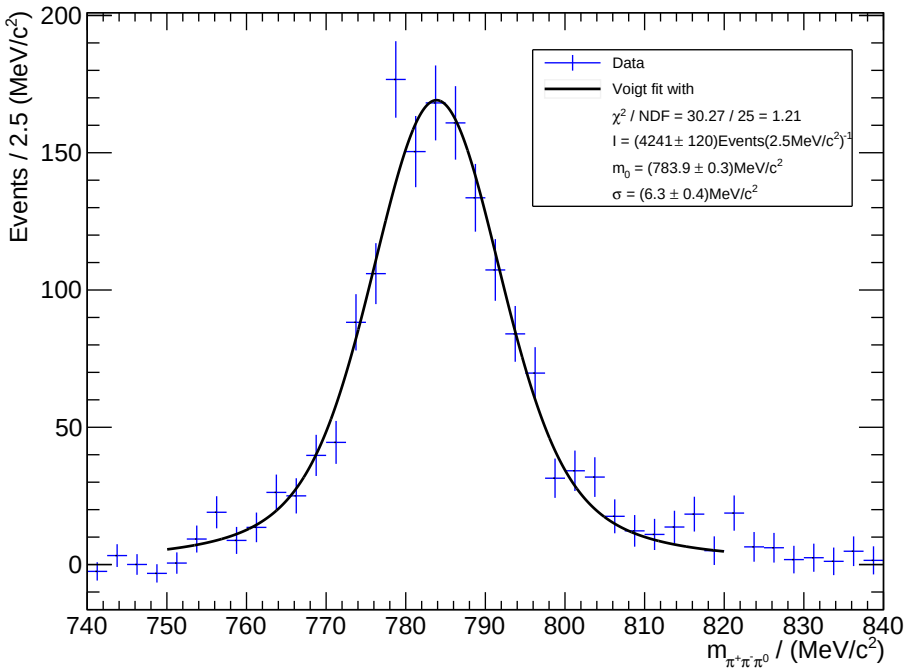

Figure 4.12 – Voigt fit to the invariant mass spectrum of the three pions for the data sample at $\sqrt{s} = (4178.4 \pm 0.8)\,\mathrm{MeV}$.

The last quantity that is needed to calculate the Born cross section σ_{Born} is the number of observed events N_{obs}. To get this number, the invariant mass spectrum of the three pions is fitted with a Voigt profile, this time for the data samples. This is shown in Figure 4.12 for the dataset at $\sqrt{s} = (4178.4 \pm 0.8)\,\mathrm{MeV}$, with parameters:

$$\begin{aligned} I &= 4241 \pm 120 \frac{\mathrm{Events}}{2\mathrm{MeV/c^2}}, \\ m_0 &= (783.9 \pm 0.3)\,\mathrm{MeV/c^2}, \\ \sigma &= (6.3 \pm 0.4)\,\mathrm{MeV/c^2}, \\ \chi^2/\mathrm{NDF} &= 30.27/25 = 1.21. \end{aligned} \tag{4.8}$$

The fits to the other datasets can be found in Appendix A.6.

Integrating over 95 % of the area of the peak gives a number of observed events of

$$N_{\text{obs}} = 1569 \pm 39. \tag{4.9}$$

According to Equation (2.15) this gives a Born cross section of

$$\sigma_{\text{Born}} = (3.17 \pm 0.10)\,\text{pb}. \tag{4.10}$$

The number of observed events N_{obs}, as well as all other determined values needed to calculate the corresponding Born cross section σ_{Born} for all datasets, can be found in Table 4.2. A plot of the Born cross section in dependence of the center-of-mass energy can be found in Figure 4.13. Here, a decrease of the cross section towards higher energies can be observed. No significant structure corresponding to a resonance can be seen. Additionally a continuum fit of the form [A$^+$17a]

$$\sigma_{\text{cont}} = \left(\frac{C}{s}\right)^{\lambda} \tag{4.11}$$

is shown. The fitted values for the parameters are

$$\begin{aligned} C &= (22.8 \pm 0.5)\,\text{pb}^{1/\lambda}\,\text{MeV}, \\ \lambda &= 4.0 \pm 0.3, \\ \chi^2/\text{NDF} &= 33.79/13 = 2.60. \end{aligned} \tag{4.12}$$

In the next step the cross section is fitted again to get upper limits on the reaction including an intermediate Y state.

Table 4.2 – Summary of the determined values needed to calculate the Born cross section for the different data samples. The values for the vacuum polarization factors have been taken from [BES15], missing ones were interpolated using a polynomial of third order.

$\sqrt{s}$/MeV	L_{int}/pb^{-1}	N_{obs}	ε/%	$(1+\delta_{\text{v}})$	$(1+\delta_{\text{r}})$	σ_{Born}/pb
4007.6 ± 0.8	482.0 ± 4.8	319 ± 17	14.60 ± 0.05	1.044 ± 0.005	1.191 ± 0.011	4.13 ± 0.24
4178.4 ± 0.8	3161.0 ± 31.8	1569 ± 39	13.10 ± 0.05	1.056 ± 0.005	1.283 ± 0.012	3.17 ± 0.10
4188.8 ± 0.8	522.5 ± 3.4	239 ± 15	13.10 ± 0.05	1.056 ± 0.005	1.291 ± 0.013	2.91 ± 0.19
4198.9 ± 0.8	524.6 ± 2.5	232 ± 15	13.07 ± 0.05	1.056 ± 0.005	1.294 ± 0.013	2.81 ± 0.19
4209.2 ± 0.8	518.1 ± 1.8	205 ± 14	12.81 ± 0.05	1.057 ± 0.005	1.292 ± 0.013	2.57 ± 0.18
4218.7 ± 0.8	514.3 ± 1.9	219 ± 14	12.86 ± 0.05	1.057 ± 0.005	1.300 ± 0.013	2.73 ± 0.19
4226.3 ± 0.7	1056.4 ± 7.1	444 ± 21	13.17 ± 0.05	1.056 ± 0.005	1.320 ± 0.013	2.60 ± 0.13
4235.7 ± 0.8	530.6 ± 2.4	196 ± 14	12.93 ± 0.05	1.056 ± 0.005	1.320 ± 0.014	2.32 ± 0.17
4243.8 ± 0.8	537.4 ± 2.6	207 ± 14	12.83 ± 0.05	1.056 ± 0.005	1.330 ± 0.013	2.42 ± 0.17
4258.0 ± 0.7	828.4 ± 5.6	336 ± 18	12.81 ± 0.05	1.054 ± 0.005	1.330 ± 0.013	2.56 ± 0.15
4266.8 ± 0.8	529.7 ± 2.8	168 ± 12	12.60 ± 0.05	1.054 ± 0.005	1.319 ± 0.014	2.05 ± 0.16
4277.7 ± 0.8	175.5 ± 0.9	43 ± 6	12.42 ± 0.05	1.053 ± 0.005	1.322 ± 0.013	1.61 ± 0.25
4358.3 ± 0.7	543.9 ± 3.7	193 ± 13	12.23 ± 0.05	1.051 ± 0.005	1.375 ± 0.014	2.28 ± 0.17
4415.6 ± 0.7	1043.9 ± 7.1	327 ± 18	11.52 ± 0.05	1.053 ± 0.005	1.412 ± 0.014	2.07 ± 0.12
4599.5 ± 0.8	586.9 ± 4.0	122 ± 11	10.35 ± 0.04	1.055 ± 0.005	1.546 ± 0.016	1.40 ± 0.13

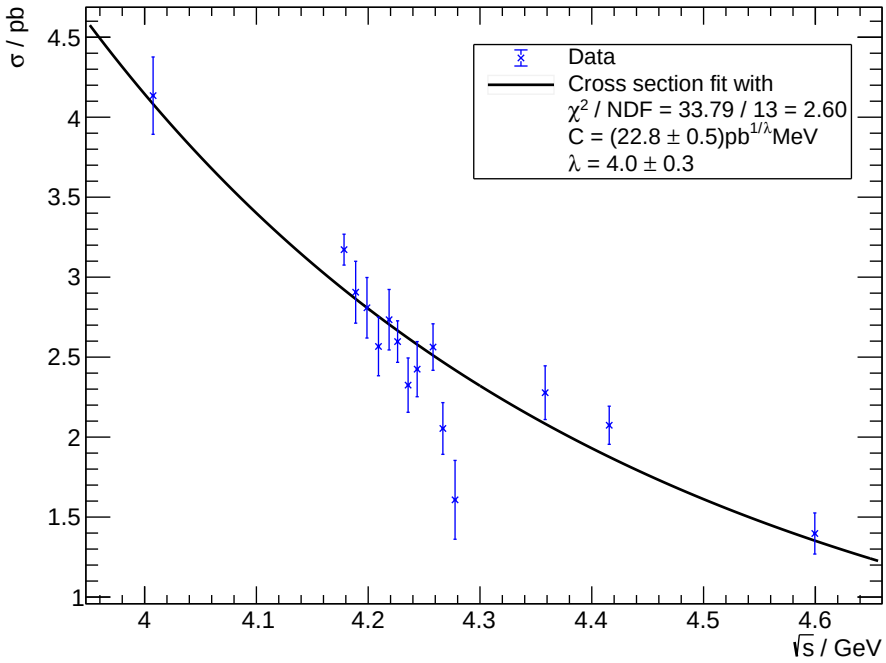

Figure 4.13 – Calculated Born cross section σ_{Born} with a fit of the form $\sigma_{\text{cont}} = \left(\frac{C}{s}\right)^{\lambda}$.

4.6 Upper limit determination of the Born cross section for $e^+e^- \to Y \to p\bar{p}\omega$

To get an upper limit for the reaction $e^+e^- \to Y \to p\bar{p}\omega$ a fit with the sum of a continuum (see Equation (4.11)) and a Breit-Wigner profile is used. On the one hand the sum is treated as a coherent sum and on the other hand as an incoherent sum of the two summands:

$$\sigma_{\text{coh}} = \left| \sqrt{\sigma_{\text{con}}} + \sqrt{\sigma_{\text{Y}}} \frac{m\Gamma}{s - m^2 + im\Gamma} \exp(i\phi) \right|^2, \tag{4.13}$$

$$\sigma_{\text{incoh}} = \sigma_{\text{con}} + \sigma_{\text{Y}} \left| \frac{m\Gamma}{s - m^2 + im\Gamma} \right|^2. \tag{4.14}$$

Here σ_{con} is the continuum cross section, σ_{Y} is the resonant cross section, which is required to be positive, m and Γ are the mass and width of a Y particle and ϕ is

a relative phase between the continuum and the Y, which is defined in the region from 0 to 2π. First these fits are done with the mass and width of the Y fixed to the PDG values of the Y(4260). This can be seen in Figure 4.14. The fitted values for the coherent sum are

$$\begin{aligned} C &= (23.6 \pm 0.6)\,\mathrm{pb}^{1/\lambda}\,\mathrm{MeV}, \\ \lambda &= 3.7 \pm 0.4, \\ \phi &= 3.9 \pm 0.3, \\ \sigma_\mathrm{Y} &= (0.018 \pm 0.010)\,\mathrm{pb}, \\ \chi^2/\mathrm{NDF} &= 20.53/11 = 1.87, \end{aligned} \tag{4.15}$$

and for the incoherent sum

$$\begin{aligned} C &= (22.8 \pm 0.5)\,\mathrm{pb}^{-\lambda}\,\mathrm{MeV}, \\ \lambda &= 4.0 \pm 0.3, \\ \sigma_\mathrm{Y} &= 0.00^{+0.023}_{-0.00}\,\mathrm{pb}, \\ \chi^2/\mathrm{NDF} &= 33.79/12 = 2.82. \end{aligned} \tag{4.16}$$

In the fit of the coherent sum σ_Y converges to a value that agrees with 0 pb within less than 2σ, so an upper limit is calculated instead of taking this as the result for the cross section. For the incoherent sum σ_Y converges to 0 pb so again an upper limit is calculated.

The coherent sum contains a possible interference between the continuum and the Y(4260) with a relative phase ϕ. Since it is possible that there are multiple continuum reactions, where the proton, antiproton and ω meson are not produced directly but via a resonance which is not the Y(4260), with possibly different relative phases, also the incoherent sum is fitted to the data. To determine the different phases a partial wave analysis would be needed.

The upper limit on the cross section σ^up for the reaction $\mathrm{e^+e^-} \to \mathrm{Y}(4260) \to \mathrm{p\bar{p}}\omega$ at the confidence level CL is calculated from the fitted values for σ_Y and its uncertainty $\Delta\sigma_\mathrm{Y}$ via [A+17a]

$$\frac{\int_0^{\sigma^\mathrm{up}} \exp\left(-\frac{(x-\sigma_\mathrm{Y})^2}{2\Delta\sigma_\mathrm{Y}}\right) \mathrm{d}x}{\int_0^{\infty} \exp\left(-\frac{(x-\sigma_\mathrm{Y})^2}{2\Delta\sigma_\mathrm{Y}}\right) \mathrm{d}x} = \mathrm{CL}. \tag{4.17}$$

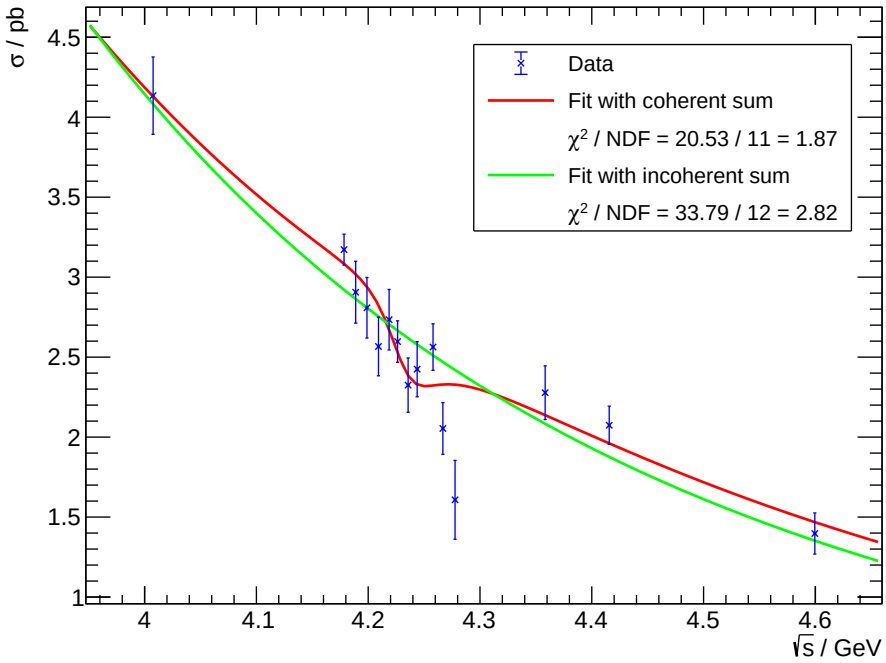

Figure 4.14 – Calculated Born cross section σ_{Born} with a fit of a coherent and an incoherent sum of the continuum and a Breit-Wigner profile.

This gives upper limits at the 90 % confidence level of

$$\sigma^{\mathrm{up}}_{\mathrm{coh}} = 0.032\,\mathrm{pb}, \tag{4.18}$$

$$\sigma^{\mathrm{up}}_{\mathrm{incoh}} = 0.037\,\mathrm{pb}. \tag{4.19}$$

In the next step the above fits are done with values of the width and mass of the Y fixed to different values. The mass is fixed to values

$$m_{\mathrm{Y},i} = 4150\,\mathrm{MeV/c^2} + i \cdot 1\,\mathrm{MeV/c^2}, \quad \text{with } i = 0, 1, \ldots, 200 \tag{4.20}$$

and the width to

$$\Gamma_{\mathrm{Y},j} = 30\,\mathrm{MeV/c^2} + j \cdot 1\,\mathrm{MeV/c^2}, \quad \text{with } j = 0, 1, \ldots, 110. \tag{4.21}$$

For each of the combinations, the upper limit at the 90 % confidence level on the Born cross section $\sigma_{\mathrm{Born}}(e^+e^- \to \mathrm{Y}(m_{\mathrm{Y},i}; \Gamma_{\mathrm{Y},j}) \to p\bar{p}\omega)$ is calculated according to

Equation (4.17). These limits can be found in Figure 4.15a for the fit with a coherent sum and in Figure 4.15b for the fit with an incoherent sum. Some sporadic outliers can be seen, which probably correspond to fits that converge to a local minimum of the χ^2 and therefore do not match the smooth behavior of the surrounding points. Additionally, the position of the Y(4260) according to the PDG [T$^+$18] is shown with its uncertainties. In both plots the Y(4260) lies in or near the minimum of the plot, which means that the best upper limit with this procedure can be given exactly for this state. The rise of the upper limit towards smaller masses can be explained by the cross section point at $\sqrt{s} = (4178.4 \pm 0.8)\,\mathrm{MeV}$ which allows narrow peaks.

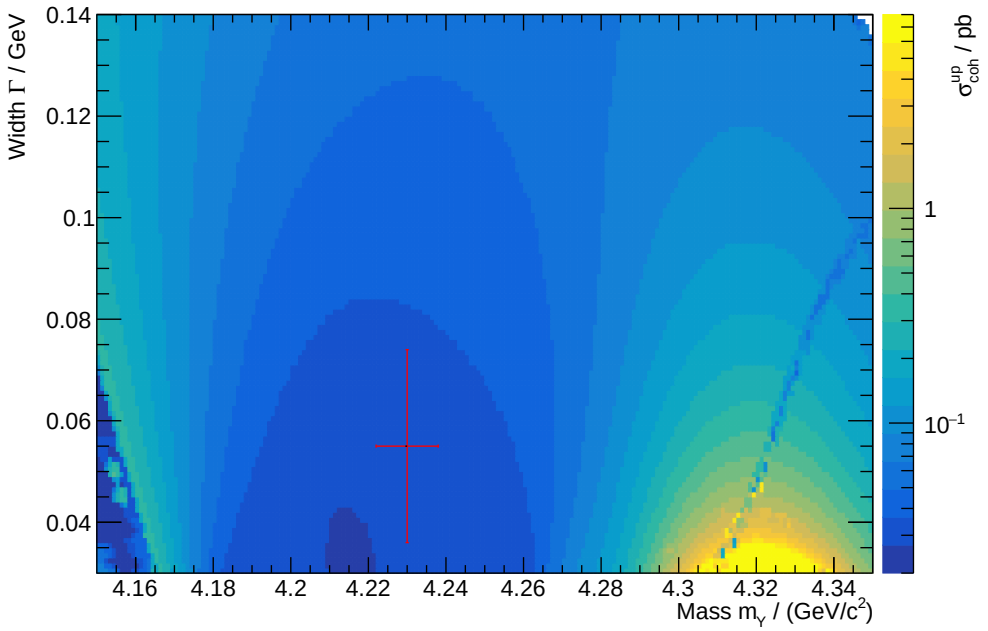

(a) Fit with coherent sum of the Breit-Wigner profile and the continuum.

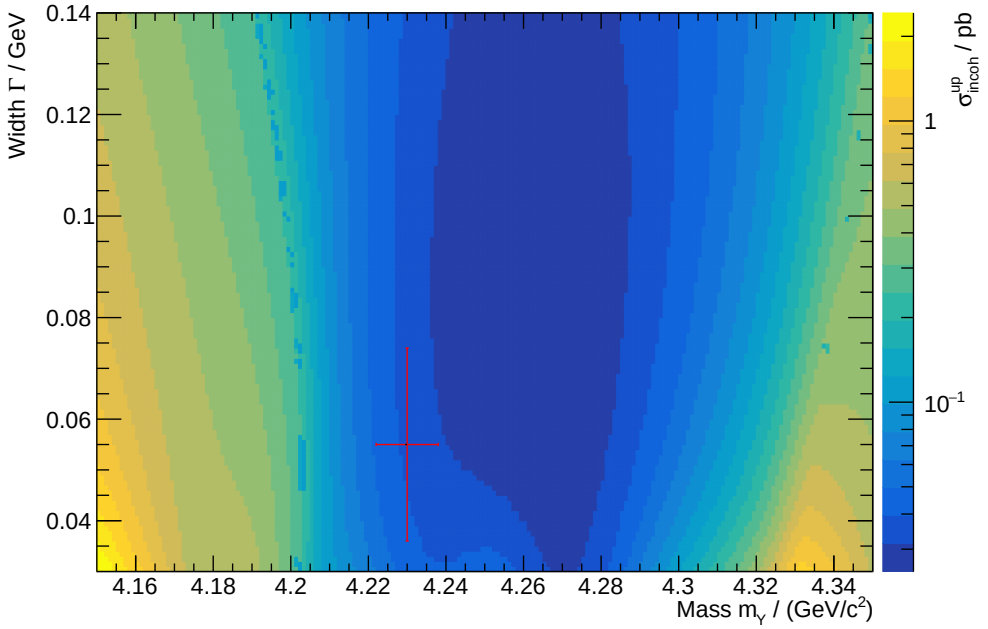

(b) Fit with incoherent sum of the Breit-Wigner profile and the continuum.

Figure 4.15 – Calculated values for the upper limits $\sigma^{\text{up}}_{\text{coh}}$ and $\sigma^{\text{up}}_{\text{incoh}}$ in dependence of the mass m_{Y} and width Γ_{Y} of the Y particle. The position of the Y(4260) according to the PDG [T+18] is highlighted.

5 Conclusion and Outlook

In this thesis the reaction $e^+e^- \to p\bar{p}\omega$ was investigated with data samples that were taken at the BESIII experiment in the period between 2011 and 2017 in the energy range from 4.0 GeV to 4.6 GeV.
The desired reaction was isolated in the data samples via basic event selection criteria and it was shown that it can be seen significantly above a remaining background. A kinematic fit was used to determine the two best γ candidates. In the inclusive Monte Carlo set a figure of merit was defined to optimize the significance of the signal above the background. Here, no maximum was observed in the FOM in dependence of the cut on the χ^2. Consequently no cut apart from convergence of the fit was applied. The background was subtracted using a quadratic fit to the $m_{\pi^+\pi^-\pi^0}$ spectrum.
The subsystems $p\bar{p}$, $p\omega$ and $\bar{p}\omega$ were studied using Dalitz plots and their projections corresponding to the invariant mass spectra of $p\bar{p}$, $p\omega$ and $\bar{p}\omega$ where $m_{p\omega}$ and $m_{\bar{p}\omega}$ were filled in the same histograms. In these spectra an enhancement at low $p\bar{p}$ invariant masses was observed. This enhancement might be produced by contributions of the particle X(1835) that was previously seen in invariant mass spectra of $p\bar{p}$ in the decay $J/\psi \to \gamma p\bar{p}$ by the BES collaboration [B$^+$03]. The width of the structure roughly matches the width reported in the PDG of $\Gamma_{X(1835)} = 242^{+14}_{-15}$ MeV [T$^+$18]. To identify additional contributions of intermediate resonances and also get detailed information on the X(1835), a partial wave analysis is necessary. In the spectrum of the $p/\bar{p}\omega$ invariant mass one might expect the presence of N^* resonances which could also be resolved by a PWA.
The ISR correction factors were determined using the event generator KKMC. Convergence of the used iterative method was observed after the third iteration. In the determination of the efficiency signal Monte Carlo samples were used and the resulting invariant mass spectrum of the three pions was fitted using a Voigt-profile. It was observed that the line shape in the simulation could not be fully described by the Voigt profile because of a small asymmetry of the peak, resulting in a relatively large

χ^2_{red}. A similar feature was seen in the spectrum gathered from the data samples. This asymmetry is probably produced by detector effects since in the signal Monte Carlo, where the ω is produced perfectly symmetric the same effect can be seen. In the behavior of the efficiency in dependence of the center of mass energy some outliers were observed which were produced by changes in the reconstruction software of the experiment.

In the last step, the number of events in the data samples was determined using again a Voigt fit. These values were then used to calculate the Born cross section $\sigma_{\text{Born}}(e^+e^- \to p\bar{p}\omega)$. The observed values are in the same order of magnitude as in similar reactions like $\sigma_{\text{Born}}(e^+e^- \to p\bar{p}\eta) = (1.80 \pm 0.13)\,\text{pb}$ [Blo18] and $\sigma_{\text{Born}}(e^+e^- \to p\bar{p}\pi^0) = (3.6 \pm 0.4)\,\text{pb}$ [A$^+$17a], each at $\sqrt{s} \approx 4190\,\text{MeV}$. To get an upper limit on the Born cross section of the reaction $e^+e^- \to Y \to p\bar{p}\omega$ a fit with a sum of a continuum and a Breit-Wigner distribution was used. The calculated upper limits for the Y(4260) were determined to be $\sigma^{\text{up}}_{\text{coh}} = 0.022\,\text{pb}$ and $\sigma^{\text{up}}_{\text{incoh}} = 0.050\,\text{pb}$, respectively. Additionally, the upper limits were calculated for varying masses and widths of a possible Y particle. Here, a smooth behavior with a few outliers was observed, with the minimum being in the vicinity of the Y(4260). The rise of the upper limits towards smaller masses can be explained by the point at $\sqrt{s} = (4178.4 \pm 0.8)\,\text{MeV}$, which allows peaks in this region.

All in all in this thesis it was possible to get a clear signal of the reaction $e^+e^- \to p\bar{p}\omega$ in the datasets used. With the obtained Born cross sections it was possible to calculate the first upper limit on the reaction $e^+e^- \to Y(4260) \to p\bar{p}\omega$. To include the possibility of identifying additional charmonium or charmonium-like states in the cross section additional high luminosity data samples at energies between 4280 MeV and 4600 MeV would be needed. Such data samples are already proposed to be taken by the BESIII experiment in the next year. Another step to improve the analysis would be the implementation of a partial wave analysis to get a better understanding of the contributing intermediate resonances, so the different phases, that would be needed for a rigorous treatment of the coherent sum of signal and background, can be extracted. Additionally, until now only statistical uncertainties were considered in the analysis, in future steps the systematic uncertainties should be determined.

A Appendix

A.1 Background fits to the $m_{\pi^+\pi^-\pi^0}$ spectra

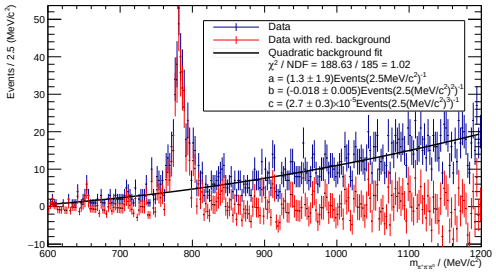

(a) Dataset 4040

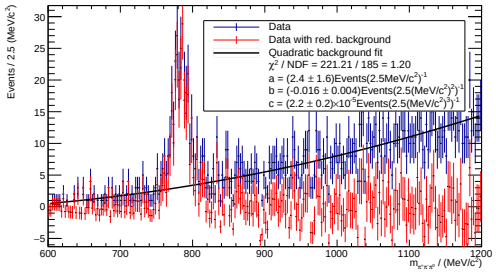

(b) Dataset 4190

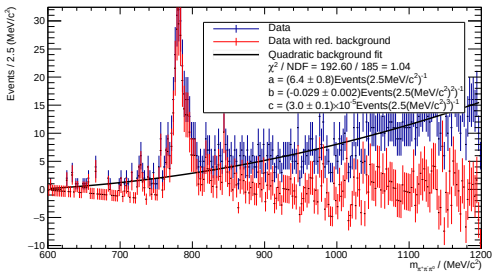

(c) Dataset 4200

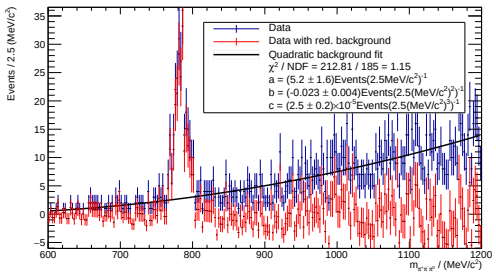

(d) Dataset 4210

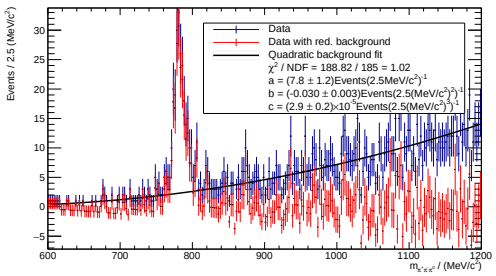

(e) Dataset 4220

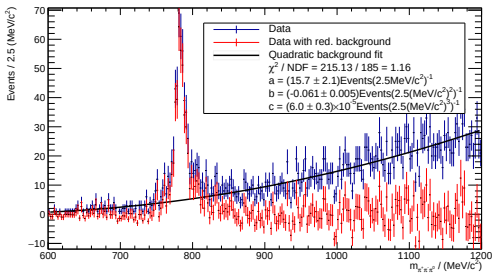

(f) Dataset 4230

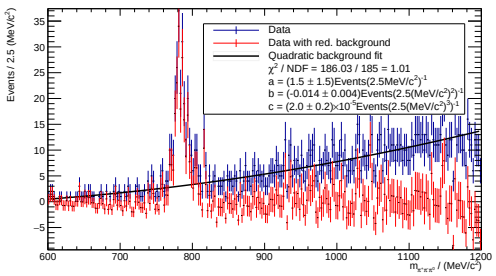

(g) Dataset 4237

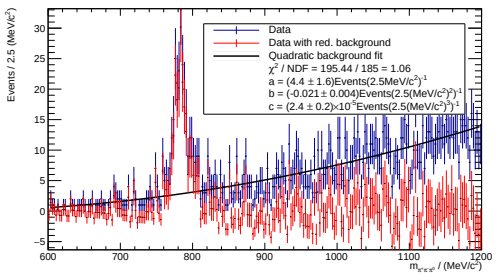

(h) Dataset 4246

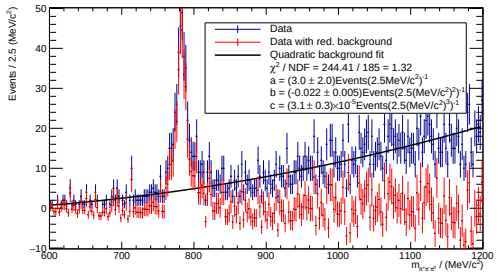

(i) Dataset 4260

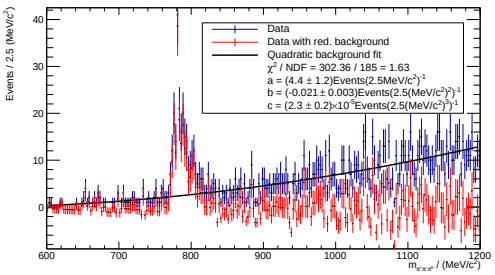

(j) Dataset 4270

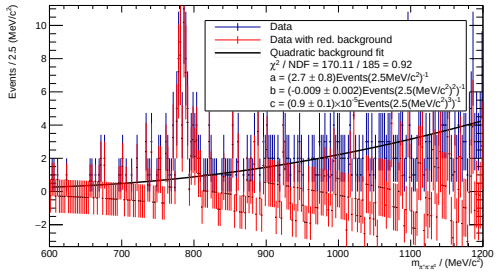

(k) Dataset 4280

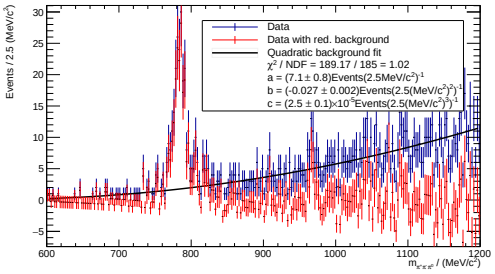

(l) Dataset 4360

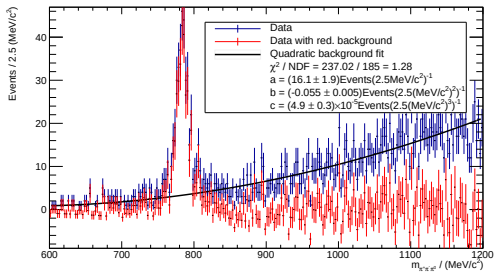

(m) Dataset 4420

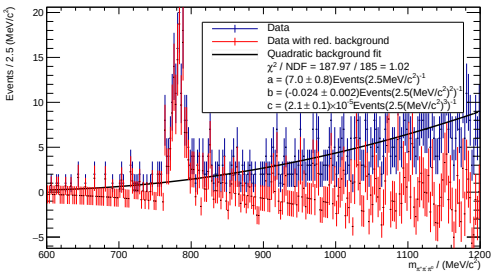

(n) Dataset 4600

Figure A.1 – Quadratic fits to the background in the $m_{\pi^+\pi^-\pi^0}$ spectra.

A.2 Dalitz plots of $m^2_{\mathrm{p}/\bar{\mathrm{p}}\omega}$ vs. $m^2_{\mathrm{p}\bar{\mathrm{p}}}$

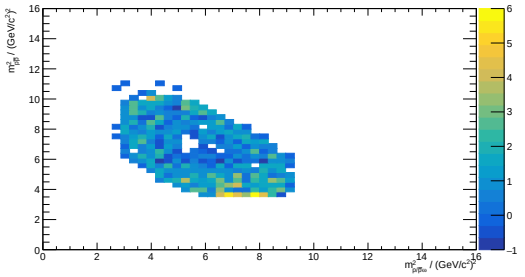

(a) Dataset 4040

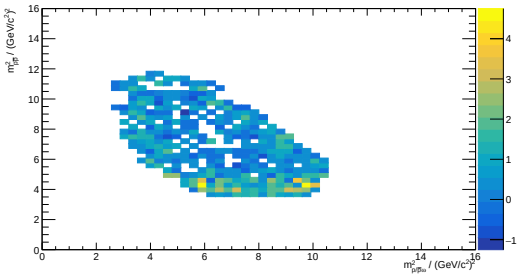

(b) Dataset 4190

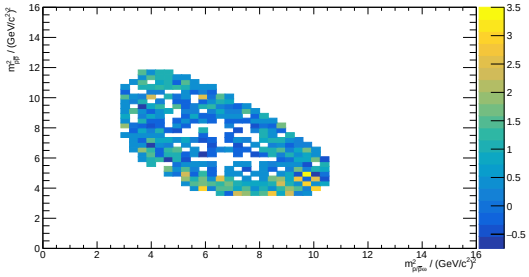

(c) Dataset 4200

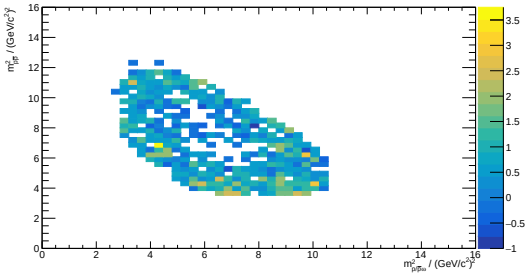

(d) Dataset 4210

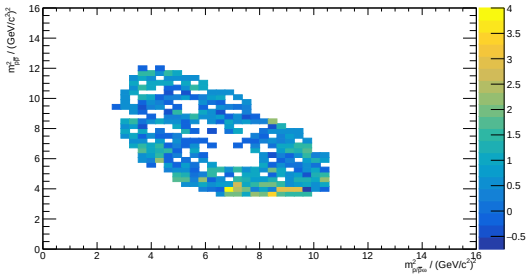

(e) Dataset 4220

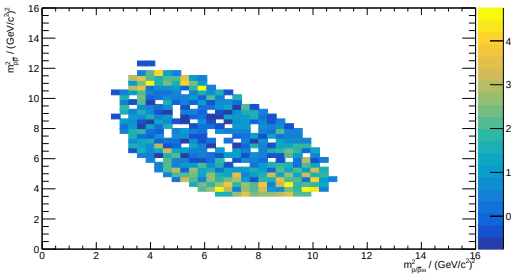

(f) Dataset 4230

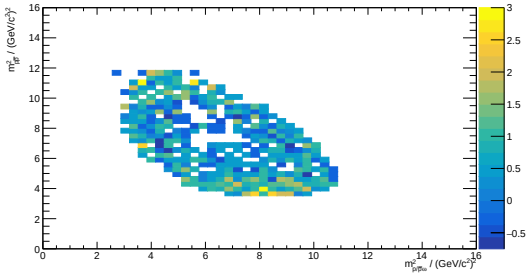

(g) Dataset 4237

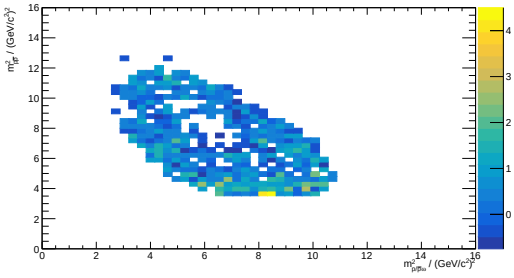

(h) Dataset 4246

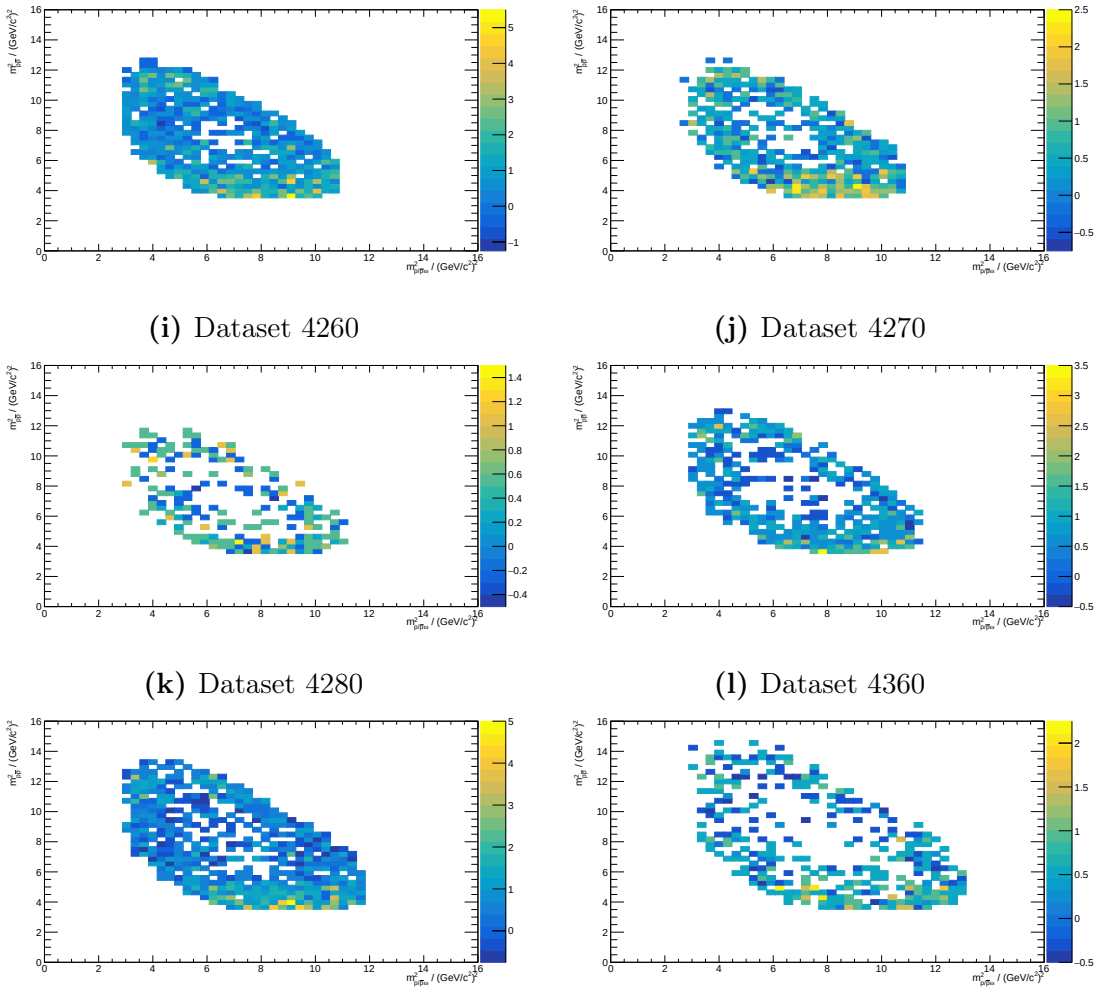

(i) Dataset 4260 **(j)** Dataset 4270

(k) Dataset 4280 **(l)** Dataset 4360

(m) Dataset 4420 **(n)** Dataset 4600

Figure A.2 – Dalitz plot with the squared invariant masses $m^2_{\mathrm{p}\omega}$ and $m^2_{\bar{\mathrm{p}}\omega}$ plotted against $m^2_{\mathrm{p}\bar{\mathrm{p}}}$.

A.3 Dalitz plots of $m^2_{\mathrm{p}\omega}$ vs. $m^2_{\bar{\mathrm{p}}\omega}$

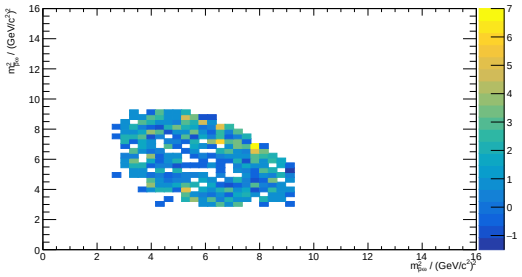

(a) Dataset 4040

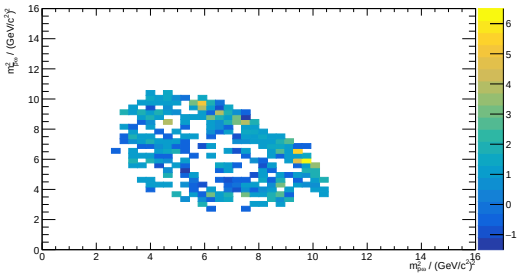

(b) Dataset 4190

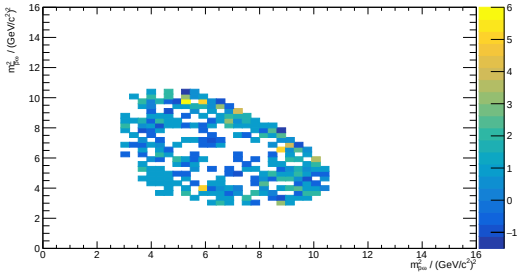

(c) Dataset 4200

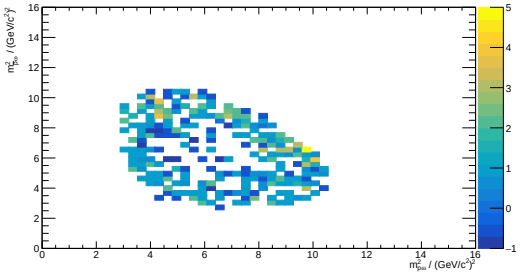

(d) Dataset 4210

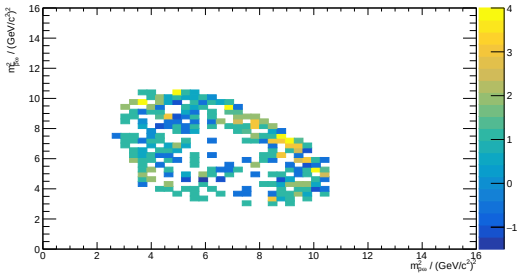

(e) Dataset 4220

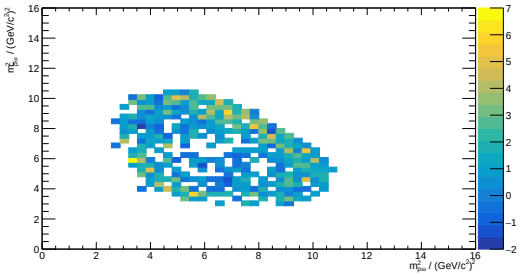

(f) Dataset 4230

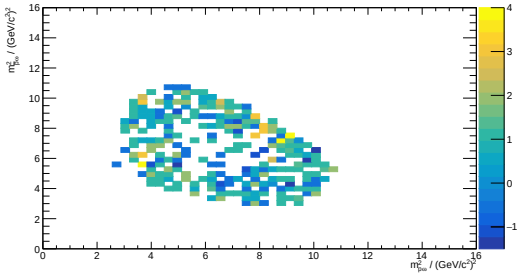

(g) Dataset 4237

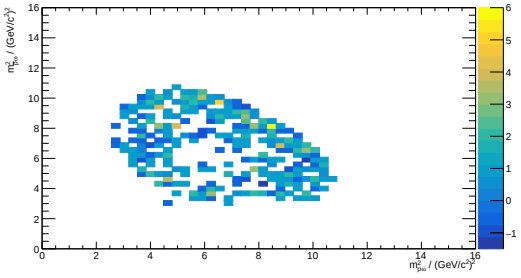

(h) Dataset 4246

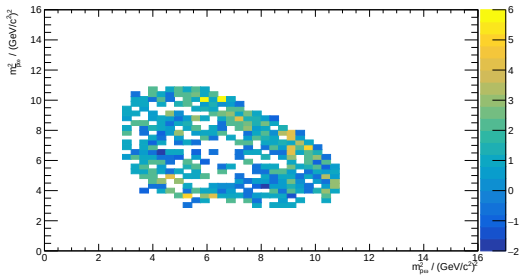

(i) Dataset 4260

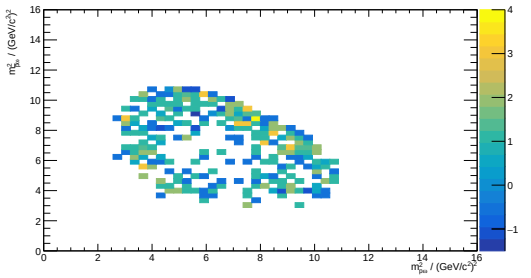

(j) Dataset 4270

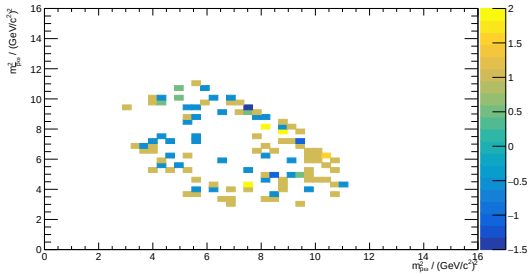

(k) Dataset 4280

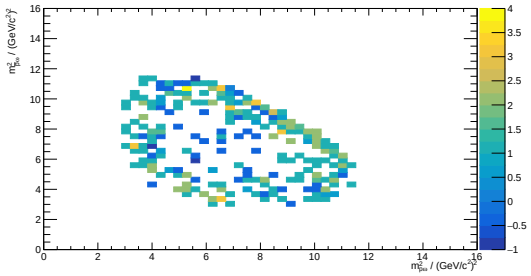

(l) Dataset 4360

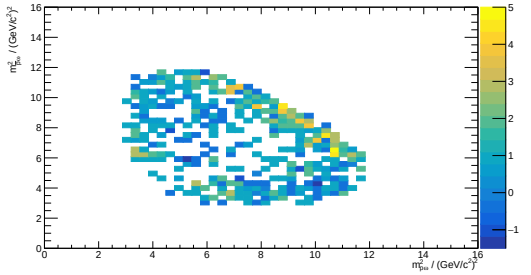

(m) Dataset 4420

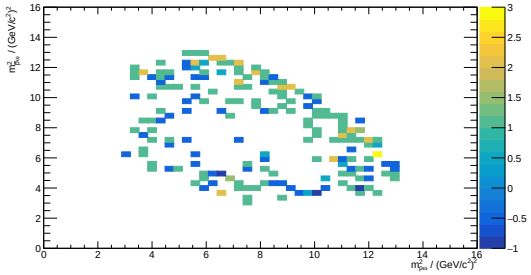

(n) Dataset 4600

Figure A.3 – Dalitz plot with the squared invariant masses $m^2_{\mathrm{p}\omega}$ and $m^2_{\bar{\mathrm{p}}\omega}$ plotted against $m^2_{\mathrm{p}\bar{\mathrm{p}}}$.

A.4 Invariant mass spectra of the p$\bar{\text{p}}$-subsystem

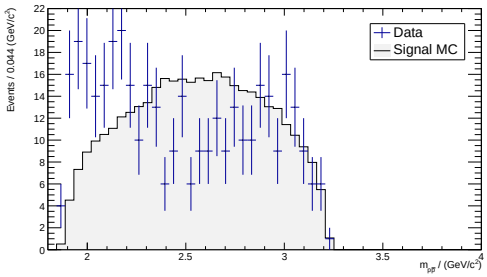

(a) Dataset 4040

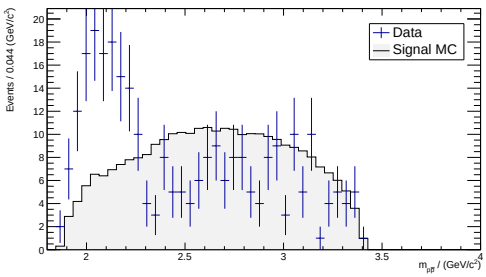

(b) Dataset 4190

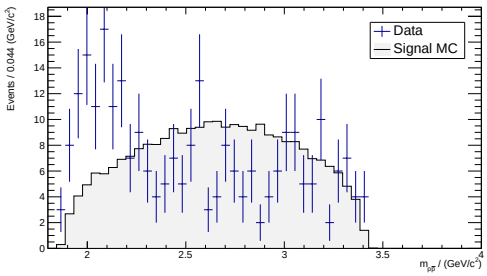

(c) Dataset 4200

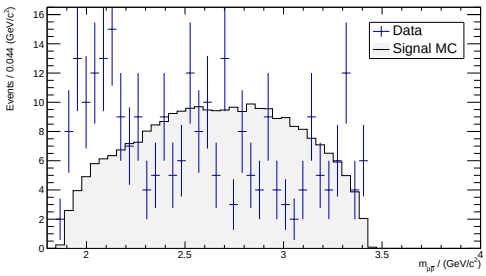

(d) Dataset 4210

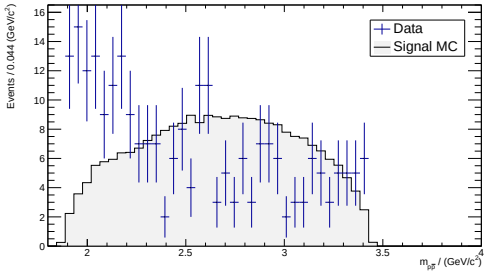

(e) Dataset 4220

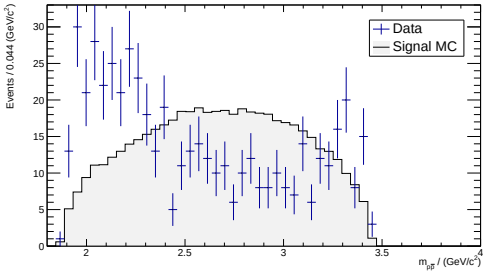

(f) Dataset 4230

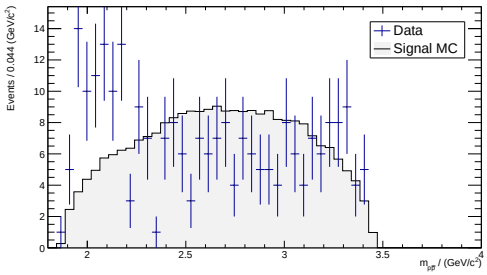

(g) Dataset 4237

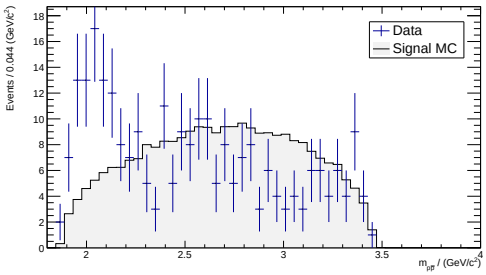

(h) Dataset 4246

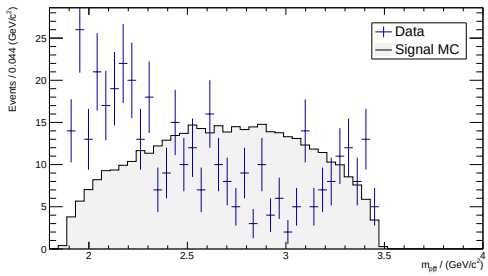

(i) Dataset 4260

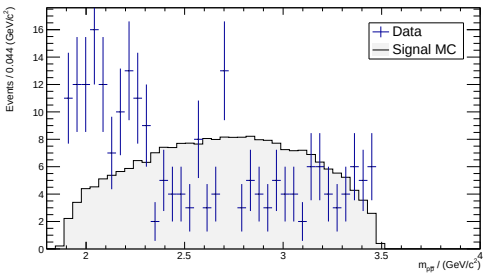

(j) Dataset 4270

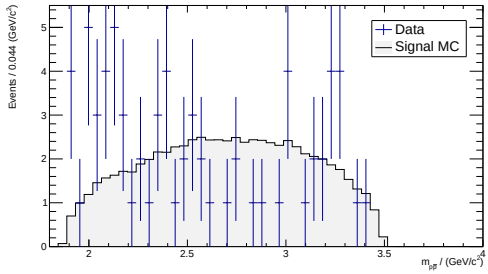

(k) Dataset 4280

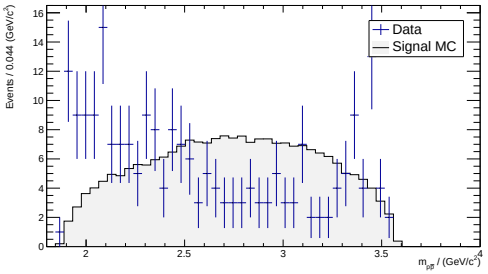

(l) Dataset 4360

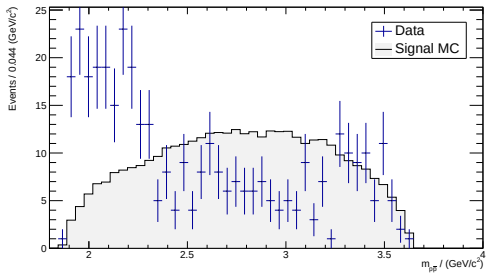

(m) Dataset 4420

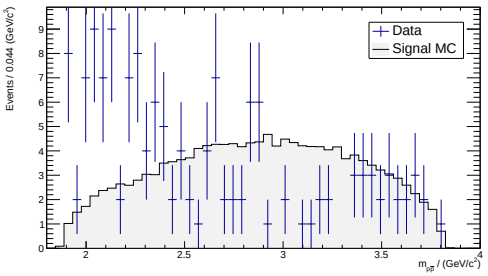

(n) Dataset 4600

Figure A.4 – Invariant mass spectra for the p$\bar{p}$-subsystem for data (blue) and for a phase space simulation (grey).

A.5 Invariant mass spectra of the pω- and p̄ω-subsystem

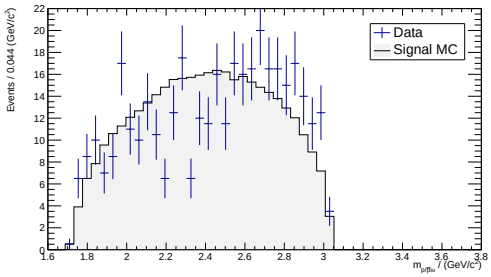

(a) Dataset 4040

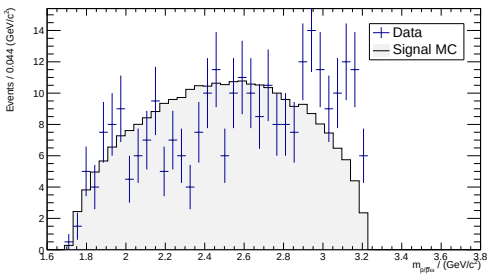

(b) Dataset 4190

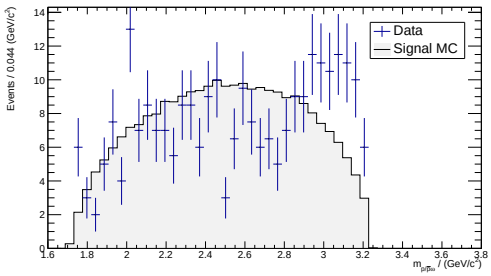

(c) Dataset 4200

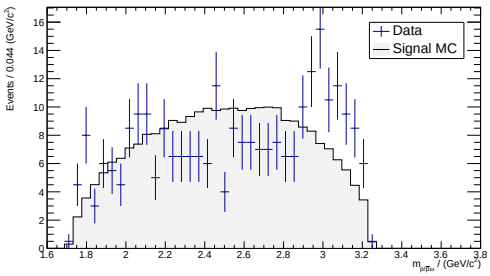

(d) Dataset 4210

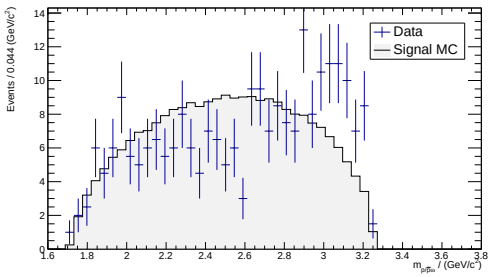

(e) Dataset 4220

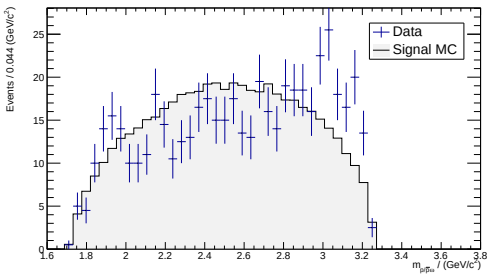

(f) Dataset 4230

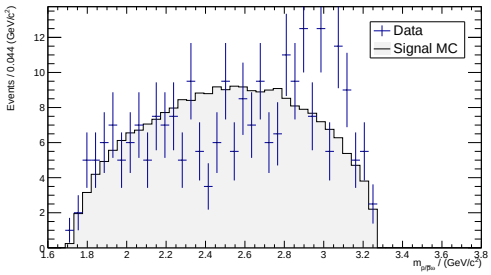

(g) Dataset 4237

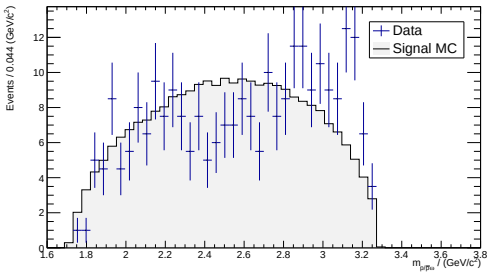

(h) Dataset 4246

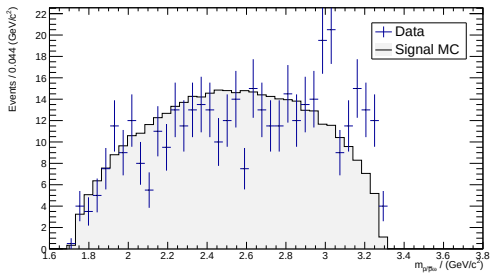

(i) Dataset 4260

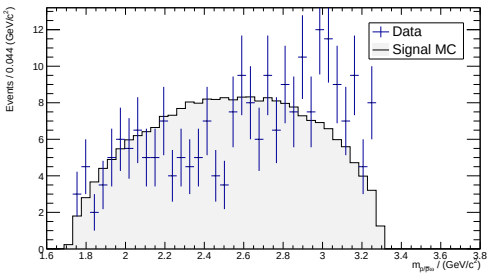

(j) Dataset 4270

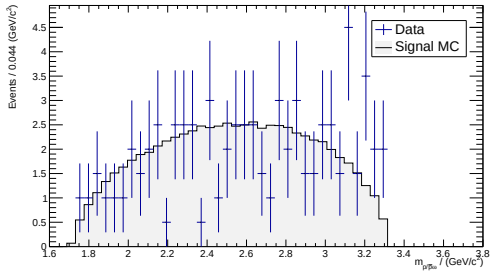

(k) Dataset 4280

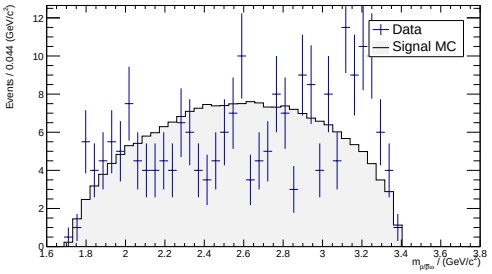

(l) Dataset 4360

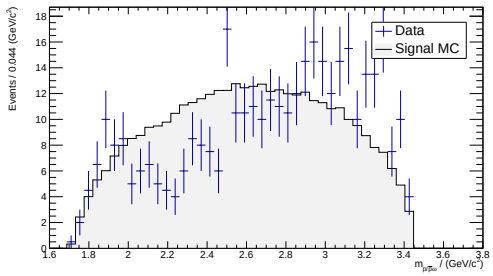

(m) Dataset 4420

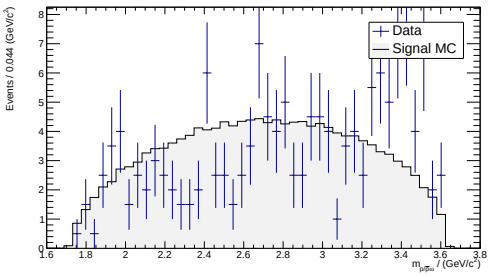

(n) Dataset 4600

Figure A.5 – Invariant mass spectra of the pω- and p̄ω-subsystem for data (blue) and for a phase space simulation (grey).

A.6 Voigt fits to the corrected $m_{\pi^+\pi^-\pi^0}$ spectra

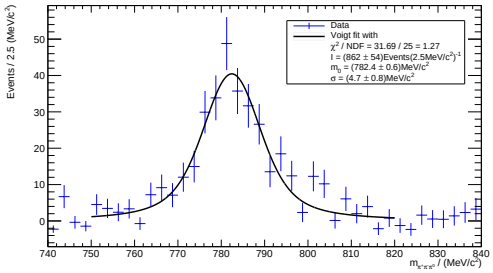

(a) Dataset 4040

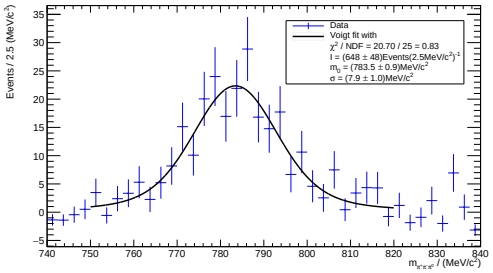

(b) Dataset 4190

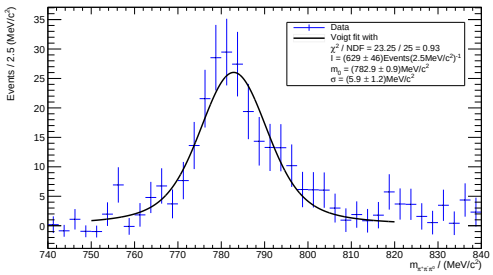

(c) Dataset 4200

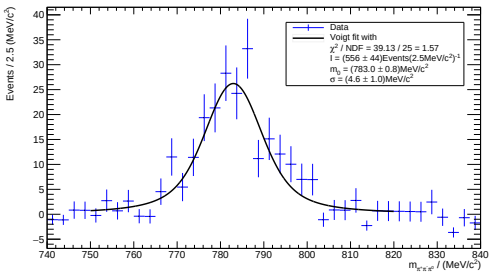

(d) Dataset 4210

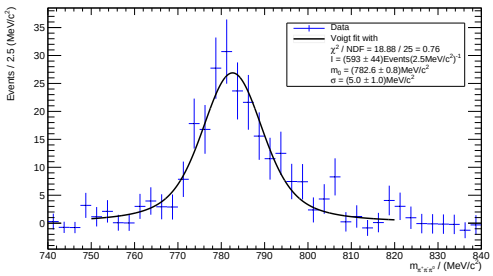

(e) Dataset 4220

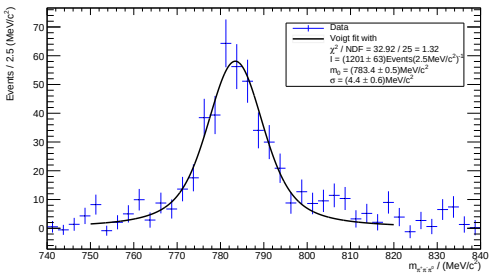

(f) Dataset 4230

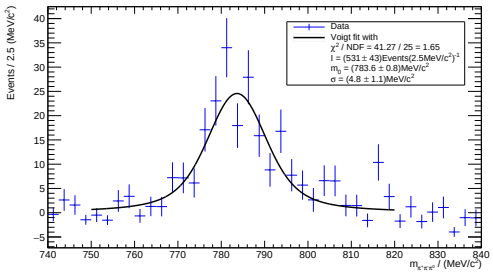

(g) Dataset 4237

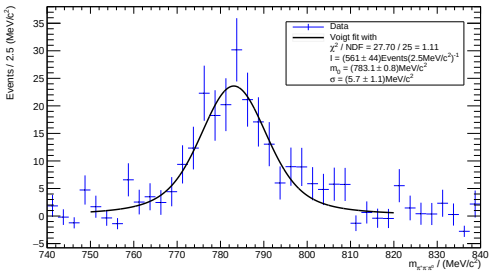

(h) Dataset 4246

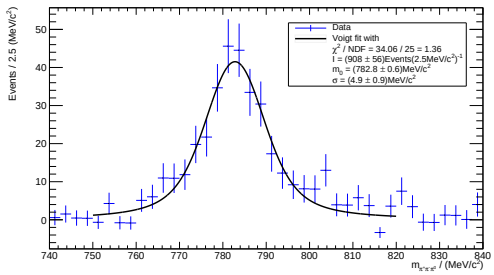

(i) Dataset 4260

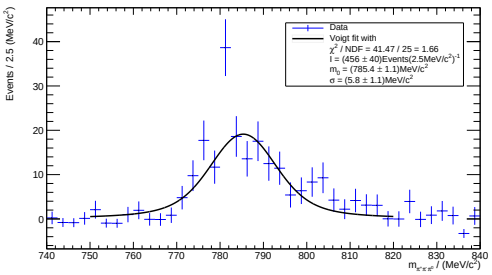

(j) Dataset 4270

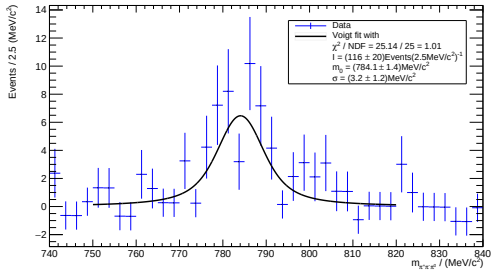

(k) Dataset 4280

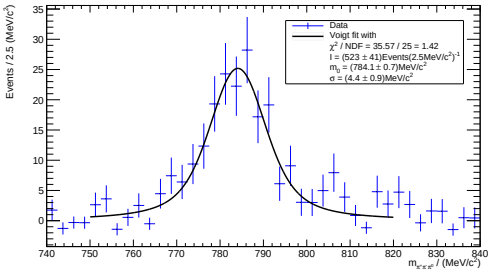

(l) Dataset 4360

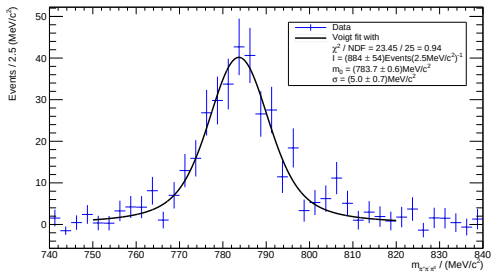

(m) Dataset 4420

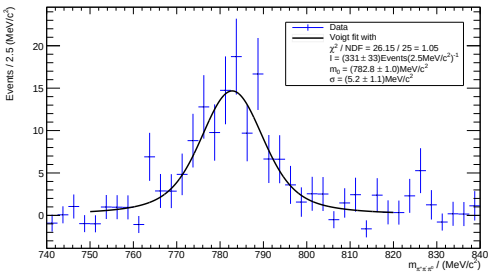

(n) Dataset 4600

Figure A.6 – Voigt fit to the invariant mass spectrum of the three pions in data.

Bibliography

[A+03] S. Agostinelli et al. *Geant4—a simulation toolkit.* Nucl. Instrum. Meth., 506(2003)(3):250–303.

[A+05a] M. Ablikim et al. (BES Collaboration). *Observation of a Resonance $X(1835)$ in $J/\psi \to \gamma\pi^+\pi^-\eta'$.* Phys. Rev. Lett., 95(2005):262001.

[A+05b] B. Aubert et al. (BABAR Collaboration). *Observation of a Broad Structure in the $\pi^+\pi^- J/\psi$ Mass Spectrum around* 4.26 GeV/c^2. Phys. Rev. Lett., 95(2005):142001.

[A+09] D. M. Asner et al. *Physics at BES-III.* Int. J. Mod. Phys., A24(2009):S1–794.

[A+10] M. Ablikim et al. (BESIII Collaboration). *Design and Construction of the BESIII Detector.* Nucl. Instrum. Meth., A614(2010):345–399.

[A+17a] M. Ablikim et al. (BESIII Collaboration). *Cross section measurements of $e^+e^- \to p\bar{p}\pi^0$ at center-of-mass energies between 4.008 and 4.600 GeV.* Phys. Lett., B771(2017):45–51.

[A+17b] M. Ablikim et al. (BESIII Collaboration). *Precise Measurement of the $e^+e^- \to \pi^+\pi^- J/\psi$ Cross Section at Center-of-Mass Energies from 3.77 to 4.60 GeV.* Phys. Rev. Lett., 118(2017):092001.

[AH99] B. Andersson and H. Hu. *Few body states in Lund string fragmentation model*, 1999. URL `https://arxiv.org/abs/hep-ph/9910285`.

[Ast20] F. W. Aston. *The constitution of atmospheric neon.* Phil. Mag Ser.6, 39(1920)(232):449–455.

[B+03] J. Z. Bai et al. (BES Collaboration). *Observation of a Near-Threshold Enhancement in the $p\bar{p}$ Mass Spectrum from Radiative $J/\psi \to \gamma p\bar{p}$ Decays.* Phys. Rev. Lett., 91(2003):022001.

[BES15] BESIII Collaboration. *The VP correction*, December 2015. Visited on 25.09.2018, URL `https://docbes3.ihep.ac.cn/~charmoniumgroup/index.php/XYZProposal`.

[Blo18] J. Bloms. *Search for exotic states in $e^+e^- \to p\bar{p}\eta$ at center-of-mass energies above 4 GeV at BES III*, 2018. Westfälische Wilhelms-Universität Münster, Institute of Nuclear Physics, Master thesis.

[C+03] S.-K. Choi et al. (Belle Collaboration). *Observation of a Narrow Charmoniumlike State in Exclusive $B^\pm \to K^\pm \pi^+ \pi^- J/\psi$ Decays.* Phys. Rev. Lett., 91(2003):262001.

[CLK08] H. S. Chung, J. Lee and D. Kang. *Cornell Potential Parameters for S-wave Heavy Quarkonia.* J. Korean Phys. Soc., 52(2008):1151–1154.

[Dal42] J. Dalton. *A New System of Chemical Philosophy.* Number 1 in A New System of Chemical Philosophy (Weale, 1842).

[Dem10] W. Demtröder. *Experimentalphysik 4.* Springer-Lehrbuch (Springer Berlin Heidelberg, 2010).

[Ele18] G. Elert. *The Physics Hypertextbook*, 2018. Visited on 23.08.2018, URL `https://physics.info/standard/`.

[Har06] F. A. Harris. *BEPCII and BESIII.* Nucl. Phys. Proc. Suppl., 162(2006):345–350.

[HT01] H. Hu and A. Tai. *Production at intermediate-energies and Lund area law.* eConf, C010430(2001):T24.

[Ins18] Institute of High Energy Physics. *BEPC & BEPCII*, 2018. Visited on 14.08.2018, URL `http://english.ihep.cas.cn/doc/1840.html`.

[Jeg11] F. Jegerlehner. *Electroweak effective couplings for future precision experiments.* Nuovo Cim., C034S1(2011):31–40.

[JWW00] S. Jadach, B. F. L. Ward and Z. Was. *The Precision Monte Carlo event generator K K for two fermion final states in e+ e- collisions*. Comput. Phys. Commun., 130(2000):260–325.

[Kel17] J. Keller. *Studies on the Y(4260) at BESIII*, 2017. Westfälische Wilhelms-Universität Münster, Institute of Nuclear Physics, Bachelor thesis.

[Kho17] A. Khoukaz. *Nuclear and Particle Physcis II*, 2017. Westfälische Wilhelms-Universität Münster, Institute of Nuclear Physics, Lecture notes.

[Mis06] MissMJ. *Standard Model of Elementary Particles*, June 2006. Visited on 19.06.2018, URL `https://commons.wikimedia.org/wiki/File:Standard_Model_of_Elementary_Particles.svg`.

[Mit14] R. Mitchell. *Efficiencies and ISR Corrections for Cross Section Measurements*, May 2014. Visited on 04.09.2018, URL `https://indico.ihep.ac.cn/event/4066/contribution/42/material/slides/0.pdf`.

[Nol10] W. Nolting. *Grundkurs Theoretische Physik 4*. Springer-Lehrbuch (Springer Berlin Heidelberg, 2010).

[NV17] V. Nesvizhevsky and J. Villain. *The discovery of the neutron and its consequences (1930–1940)*. Comptes Rendus Physique, 18(2017)(9):592 – 600.

[Ols15] S. L. Olsen. *XYZ Meson Spectroscopy*. In: *Proceedings, 53rd International Winter Meeting on Nuclear Physics (Bormio 2015)* (2015) .

[Pin08] R.-G. Ping. *Event generators at BESIII*. Chin. Phys., C32(2008):599.

[PP07] R. G. Ping and C. Y. Pang. *Monte Carlo Generators for Tau-Charm-Physics at BESIII*, July 2007. Visited on 06.09.2018, URL `https://docbes3.ihep.ac.cn/~offlinesoftware/images/6/6a/Guide_BesEvtGen.pdf`.

[R+07] A. Ryd et al. *EvtGen. A Monte Carlo Generator for B-Physics*, September 2007. Visited on 10.09.2018, URL `https://docbes3.ihep.ac.cn/~offlinesoftware/images/6/63/Guide_EvtGen.pdf`.

[Rut11] E. Rutherford. *The scattering of alpha and beta particles by matter and the structure of the atom.* Phil. Mag. Ser.6, 21(1911):669–688.

[T+18] M. Tanabashi et al. *Review of Particle Physics* (Particle Data Group, 2018). Phys. Rev. D, 98:030001.

[Uni10] University of Minnesota. *BES III*, 2010. Visited on 14.08.2018, URL `http://www.hep.umn.edu/bes3/`.

[Won98] S. Wong. *Introductory Nuclear Physics.* A Wiley-Interscience publication (Wiley, 1998).

[Zwe09] P. Zweber (BESIII Collaboration). *Charm Factories: Present and Future.* AIP Conf. Proc., 1182(2009):406–409.

Acknowledgements

I thank all the people that supported me during the preparation of my master thesis. In particular my thanks go to Prof. Dr. Alfons Khoukaz for the warm inclusion to the working group, as well as the friendly and objective support during preparation of the thesis. I thank Dr. Volker Hannen for being my second reviser.
A special thank also goes to Marcel and Nils for the supervision during my daily work on the thesis and all the helpful comments on programming mistakes and physics questions.
A hearty thanks goes to my complete working group for the warm and friendly working environment and all the times we laughed together about our Johannes figurine.

Eidesstattliche Erklärung

Ich versichere an Eides statt durch meine Unterschrift, dass ich die vorstehende Arbeit selbständig angefertigt und alle Aussagen, die ich wörtlich oder annähernd wörtlich aus Veröffentlichungen entnommen habe, als solche kenntlich gemacht habe, mich auch keinerlei anderer als der angegebenen Literatur oder sonstiger Hilfsmittel bedient habe. Die Arbeit hat in dieser oder ähnlicher Form noch keiner anderen Prüfungsbehörde vorgelegen.

(Datum, Unterschrift)

Ich erkläre mich mit einem Abgleich der Arbeit mit anderen Texten zwecks Auffindung von Übereinstimmungen sowie mit einer zu diesem Zweck vorzunehmenden Speicherung der Arbeit in eine Datenbank einverstanden.

(Datum, Unterschrift)